



# Electron-rich Cu<sup>0</sup>-Cu<sub>2</sub>O heterogeneous interface constructed via controllable electrochemical reconstruction for a single CO<sub>2</sub> deep-reduction product ethylene

WeiQi Liu, Peiyao Bai, Shilin Wei, Xiao Kong, Chuangchuang Yang, Lang Xu<sup>\*</sup>

MOE Key Laboratory of Coal Processing and Efficient Utilization, School of Chemical Engineering and Technology, China University of Mining and Technology, 1 Daxue Road, Xuzhou, Jiangsu 221116, China

## ARTICLE INFO

### Keywords:

External Cu<sub>2</sub>O  
Internal Cu<sup>0</sup>  
Heterostructure  
Local electron density  
Strong tendency to C<sub>2</sub>H<sub>4</sub>

## ABSTRACT

Present Cu-based catalysts are prone to yield various reduction products and small current densities in electrocatalytic CO<sub>2</sub> reduction. We now construct heterostructured Cu<sup>0</sup>-Cu<sub>2</sub>O nanoparticles on the surface of coal matrix using electrochemical reconstruction and PTFE surface modification. The introduction of PTFE modulates the reconstruction process and induces the exposure of only a single-type Cu<sub>2</sub>O crystal on its surface, leading to a single deep-reduction product ethylene accordingly. The electron-rich heterogeneous interface formed by internal Cu<sup>0</sup> and external Cu<sub>2</sub>O optimizes the local electron density of surface Cu<sub>2</sub>O active sites, promoting the rapid protonation of \*CO to \*CHO and improving the catalytic tendency toward ethylene. The combination of highly conductive and robust coal matrix with hydrophobic PTFE suppresses competing side reactions and enhances the catalytic activity and selectivity to ethylene. Consequently, the Cu-based catalyst achieves the enhanced tendency for ethylene (93%), faradaic efficiency (62%) and industrial-grade current density (142.4 mA cm<sup>-2</sup>).

## 1. Introduction

Electrocatalytic CO<sub>2</sub> reduction (ECR), which can be driven by renewable energy sources to transform CO<sub>2</sub> into high value-added deep-reduction products, is a promising strategy to diminish human dependence on fossil fuels and thus to achieve rapid decarbonization [1–4]. However, most of present catalysts are only capable of producing CO due to their weak adsorption capabilities for the important intermediate \*CO in the ECR processes [5–7]. Fortunately, Cu-based catalysts with moderate adsorption strengths for \*CO are able to promote further protonation and C-C coupling reactions of \*CO, which can in turn convert CO<sub>2</sub> to deep-reduction products [8–11]. Among all deep-reduction products, ethylene (C<sub>2</sub>H<sub>4</sub>) is particularly valuable because it is one of the most important building blocks in the chemical industry [12,13].

However, conventional polycrystalline Cu catalysts have poor ECR product selectivities, and some of \*CO inevitably desorbs from active sites during the reactions. These behavioral features result in the production of a variety of hydrocarbons and oxygenates, ranging from C<sub>1</sub> to C<sub>2</sub> and even C<sub>3</sub> compounds, which not only increases the cost of product

separation but also leads to the poor tendency of the catalysts to form C<sub>2</sub>H<sub>4</sub> [14,15]. Since current density can reflect the electrocatalytic activity of a sample [16], we quantitatively analyze its tendency toward C<sub>2</sub>H<sub>4</sub> using the ratio ( $\alpha$ ) of C<sub>2</sub>H<sub>4</sub> partial current density ( $j_{C_2H_4}$ ) to total current density of ECR products ( $j_{ECR}$ ), i.e.,

$$\alpha = \frac{j_{C_2H_4}}{j_{ECR}} \quad (1)$$

According to Eq. 1, it is clear that a Cu-based sample with a higher  $j_{C_2H_4}$  and fewer ECR product species would have a greater  $\alpha$  value (increasing tendency for C<sub>2</sub>H<sub>4</sub>). At present, oxide-derived Cu (abbreviated OD Cu, composed of Cu<sub>2</sub>O and metallic Cu<sup>0</sup>) catalysts synthesized by electrochemical reconstruction have been widely reported because of their relatively high faradaic efficiencies of C<sub>2</sub> products [17–19]. A synergistic effect exerted by Cu<sub>2</sub>O and Cu<sup>0</sup> can significantly reduce activation energy barriers of CO<sub>2</sub> molecules and promote C-C coupling reactions on OD Cu surfaces, thereby effectively inhibiting the formation of C<sub>1</sub> products such as methane and methanol [20,21]. Therefore, the catalytic activity and C<sub>2</sub>H<sub>4</sub> tendency of this mixed-active-site structure are superior to those of pure Cu<sup>0</sup> or Cu<sub>2</sub>O [22,23]. However, the complex

<sup>\*</sup> Corresponding author.

E-mail address: [lang.xu@cumt.edu.cn](mailto:lang.xu@cumt.edu.cn) (L. Xu).

<https://doi.org/10.1016/j.apcatb.2024.123831>

Received 8 November 2023; Received in revised form 3 February 2024; Accepted 8 February 2024

Available online 15 February 2024

0926-3373/© 2024 Elsevier B.V. All rights reserved.

electrochemical reconstruction process of OD Cu makes it difficult for researchers to precisely tailor its active-site structure, which results in the exposure of both  $\text{Cu}_2\text{O}$  and  $\text{Cu}^0$  on the surface of the previously reported OD Cu catalysts [17–19]. Because the mixed-active-site structure on the surface of OD Cu leads to the similar activation energy barriers for reaction intermediates of  $\text{C}_2\text{H}_4$  and  $\text{CH}_3\text{CH}_2\text{OH}$ , OD Cu would give rise to  $\text{C}_2\text{H}_4$  and  $\text{CH}_3\text{CH}_2\text{OH}$  simultaneously as the mixed products [24]. Hence, the  $\alpha$  values of the previously reported OD Cu catalysts can hardly exceed 70%, resulting in the unsatisfactory  $\text{C}_2\text{H}_4$  tendencies (Table S1). Given that a catalyst possessing a single-type active-site structure tends to produce one kind of reduction product [25,26], we need to precisely regulate the reconstruction process of OD Cu and make it only expose one single-type active-site structure. This strategy is conducive to modulating the difference in activation energy barriers of reaction intermediates of  $\text{C}_2\text{H}_4$  and  $\text{CH}_3\text{CH}_2\text{OH}$  on the surface of OD Cu, thus resulting in a strong bias toward one desired product (in this case  $\text{C}_2\text{H}_4$ ) that is more thermodynamically favorable. Therefore, the single-type active-site structure allows OD Cu to obtain the single deep-reduction product  $\text{C}_2\text{H}_4$  and to achieve the strong tendency toward  $\text{C}_2\text{H}_4$ .

Polytetrafluoroethylene (PTFE) is often used to modify ECR catalysts because of its excellent hydrophobicity, which can significantly inhibit an unwanted side reaction, known as hydrogen evolution reaction (HER) [27,28]. It is worth noting that PTFE also possesses the characteristics of stable structure and low electrical conductivity. The reason why it is difficult to precisely tailor the active-site structure of the above-mentioned OD Cu is that the reduction kinetics of  $\text{Cu}^{\delta+}$  ( $\delta = 1$  or 2) is too rapid [29]. Therefore, the introduction of low-conductivity PTFE into OD Cu should be able to lower the reduction kinetics of Cu species and to control the reconstruction process, thereby making it more favorable to generate one single-type active-site structure. On the other hand, the low electrical conductivity of PTFE would increase the electrocatalyst resistance, thus causing low current density. Fortunately, the negative impact of PTFE can be offset by incorporating a coal matrix into the catalyst, because the robust carbon skeleton of coal matrix possesses an outstanding electrical conductivity and can considerably raise the electron-transfer rate [30,31]. Also noteworthy, the spatial confinement of micropores in the coal matrix is able to reduce the aggregation of metal species and to elevate the number of active sites, which thus helps to increase the catalytic rate [31]. To the best of our knowledge, tailoring the active-site structure of OD Cu with PTFE and increasing the  $j_{\text{C}_2\text{H}_4}$  of OD Cu with the coal matrix have not been investigated systematically.

It should be noted that the intrinsic activity of a Cu-based catalyst with a single-type active-site structure is relatively low, which gives rise to the weak tendency toward  $\text{C}_2\text{H}_4$  and the high overpotential [22]. Accordingly, it is necessary to incorporate a second active species into the primary one to optimize the electronic structure of the latter and to exploit the synergistic effect of both species, which in turn strengthens the electrochemical performance of the catalyst [32–35]. As mentioned earlier, however, the simultaneous exposure of two active species on the OD Cu surface tends to generate multiple deep-reduction products during the ECR, hence leading to a low tendency toward  $\text{C}_2\text{H}_4$  [24,36]. Therefore, burying the second active species deeply within the catalyst to form a heterostructure is an excellent strategy for making a catalyst showing a high bias in favor of  $\text{C}_2\text{H}_4$ , because this kind of structure can not only avoid the direct contact of the second active species with  $\text{CO}_2$  and intermediates to inhibit by-product generations but also allow the second active species to engineer the electronic structure of surface active sites, thereby optimizing the activation energy barriers for intermediates of the product  $\text{C}_2\text{H}_4$  and realizing the strong tendency toward  $\text{C}_2\text{H}_4$ . Accordingly, if the Cu-based heterostructure of this type can be available, then the problems of low  $\alpha$  values and multiple reduction products generated by mixed active sites will be solved, and highly active ECR catalysts that efficiently generate the single deep-reduction product  $\text{C}_2\text{H}_4$  will also be obtained.

In this work we successfully synthesize heterostructured  $\text{Cu}^0\text{-Cu}_2\text{O}$  nanoparticles on the surface of porous coal matrix using electrochemical reconstruction and surface modification with PTFE, in which  $\text{Cu}_2\text{O}$  is exposed on the nanoparticle surface whereas  $\text{Cu}^0$  is encapsulated inside  $\text{Cu}_2\text{O}$ . PTFE lowers the electron accumulation near the  $\text{Cu}_2\text{O}$  species on the surface, thus protecting them from further electrochemical reduction, while the Cu species buried within  $\text{Cu}_2\text{O}$  are readily reduced to  $\text{Cu}^0$  due to their lack of contact with PTFE. Physicochemical characterization and theoretical simulation results show that the  $\text{Cu}^0\text{-Cu}_2\text{O}$  heterostructure with a single-type  $\text{Cu}_2\text{O}$  active-site structure exposed on its surface allows the targeted conversion of  $^*\text{CO}$  to  $^*\text{CHO}$ , a key intermediate for  $\text{C}_2\text{H}_4$  in the ECR process, therefore realizing the generation of the single deep-reduction product  $\text{C}_2\text{H}_4$ . In addition, the internal  $\text{Cu}^0$  forms an electron-rich heterogeneous interface with external  $\text{Cu}_2\text{O}$ , which engineers the local electron density of  $\text{Cu}^+$  sites of the surface  $\text{Cu}_2\text{O}$  species, optimizes the adsorption strength of the  $\text{Cu}^+$  sites with  $^*\text{CO}$ , and thus lowers the thermodynamic energy barrier for the protonation of  $^*\text{CO}$  to  $^*\text{CHO}$ . The coal matrix not only effectively suppresses the coalescence degree of  $\text{Cu}^0\text{-Cu}_2\text{O}$  nanoparticles during the electrochemical reconstruction and increase the number of active sites by virtue of its spatial confinement effect, but also significantly elevate the  $j_{\text{C}_2\text{H}_4}$  thanks to its robust carbon skeleton as well as its excellent conductivity. Altogether, the unique ternary component, the highly active  $\text{Cu}^0\text{-Cu}_2\text{O}$  heterostructure and the electron-rich heterogeneous interface prompt the catalyst to yield a large  $\alpha$  value of 93%, reflecting its outstanding tendency toward  $\text{C}_2\text{H}_4$ . Moreover, the catalyst achieves  $142.4 \text{ mA cm}^{-2}$  industrial-grade  $\text{C}_2\text{H}_4$  partial current density, 62%  $\text{C}_2\text{H}_4$  faradaic efficiency and 20 h stability in a flow cell, which indeed has great potential for industrial applications. Therefore, this study offers an alternative approach for highly active and selective electrocatalysts to produce  $\text{C}_2\text{H}_4$  via the ECR route.

## 2. Experimental section

### 2.1. Synthesis of porous coal

3 g of anthracite coal (Taixi anthracite) was placed in a ball mill (CSSQM-1) and treated at 400 rpm for 2 h, and then washed with 3 M KOH and 1 M HCl at 60 °C for 2 h sequentially. Later, 0.3 g of clean anthracite coal and 0.9 g of KOH were added to a solution consisting of 5 mL of water and 5 mL of ethanol, and the resulting mixture was heated to 80 °C and stirred vigorously. After the solvent evaporated, the mixture was placed in a vacuum oven at 80 °C for 12 h. Next, the black solid was transferred to a tube furnace and heated to 750 °C at a heating rate of 5 °C  $\text{min}^{-1}$  ( $\text{N}_2$  atmosphere) and held at this temperature for 30 min. The obtained black powder was rinsed with 1 M HCl at 60 °C for 2 h. The mixture was then treated with suction filtration and washed thoroughly with deionized water. The as-prepared porous coal (named PC) was dried in an oven overnight (80 °C).

### 2.2. Synthesis of $\text{Cu}_x\text{O}$ precursor

0.1 g of PC, 0.48 g of  $\text{Cu}_2(\text{NO}_3)_2 \cdot 3 \text{H}_2\text{O}$ , 1 mL of polyoxyethylene alkyl ether, 0.5 g of PTFE, and 0.5 mL of ethanol were added together to 50 mL of deionized water, and the resulting mixture was heated to 55 °C and stirred vigorously for half an hour. Afterward, 0.5 g of NaOH was added to the mixture. After stirring for half an hour, a certain quantity of ascorbic acid was added to the above mixed solution. Then, the mixture was further stirred at 55 °C for 30 min. The resulting precipitate was separated by centrifugation and washed with deionized water for three times. Finally, the obtained  $\text{Cu}_x\text{O}$  precursor was dried in an oven at 80 °C for 12 h. The  $\text{Cu}_x\text{O}$  precursors obtained by using 0.01, 0.05, and 0.1 g of ascorbic acid were called C/Cu/PTFE-0.01, C/Cu/PTFE-0.05, and C/Cu/PTFE-0.1, respectively. In order to study the effects of PC and PTFE on the electrochemical properties of the catalysts, we prepared Cu/PTFE-0.05 and C/Cu-0.05 according to the synthesis method for C/Cu/

PTFE-0.05, where no PC was used in the preparation of Cu/PTFE-0.05 and no PTFE was used in the preparation of C/Cu-0.05.

### 2.3. Synthesis of heterostructured $\text{Cu}^0\text{-Cu}_2\text{O}$ catalyst

10 mg of  $\text{Cu}_x\text{O}$  precursor and 20  $\mu\text{L}$  of Nafion solution were added to 980  $\mu\text{L}$  of isopropanol, followed by ultrasonication for 1 h to obtain a well-mixed slurry. Afterward, the mixed solution was evenly dropped onto the carbon paper with a sample loading of approximately  $1\text{ mg cm}^{-2}$ . An electrochemical reconstruction was undertaken in a three-electrode H-type cell with carbon paper, platinum sheet, and Ag/AgCl (3.5 M KCl) electrode as the working, counter, and reference electrodes, respectively. The electrolyte was a  $\text{CO}_2$ -saturated 0.5 M  $\text{KHCO}_3$  solution. The  $\text{Cu}^0\text{-Cu}_2\text{O}$  nanoparticulate catalyst with a heterostructure was obtained by treating the working electrode at a constant potential ( $-1.0\text{ V}$  vs. reversible hydrogen electrode, RHE) for half an hour. The catalysts obtained from C/Cu/PTFE-0.01, C/Cu/PTFE-0.05, C/Cu/PTFE-0.1, Cu/PTFE-0.05, and C/Cu-0.05 were denoted C/Cu/PTFE-0.01-R, C/Cu/PTFE-0.05-R, C/Cu/PTFE-0.1-R, Cu/PTFE-0.05-R, and C/Cu-0.05-R, respectively. These catalysts can directly be used for electrochemical performance testing. In addition, the catalysts removed from the carbon paper surface by ultrasonication can be used for other characterization measurements.

### 2.4. Material characterization

Transmission electron microscopy (TEM) images were recorded on a FEI Talos F200x G2 transmission electron microscope operated at an acceleration voltage of 200 kV. Energy dispersive spectroscopy (EDS) elemental mapping images were obtained by EDS Super-X instrumentation equipped on the FEI Talos F200x G2 with an acceleration voltage of 200 kV and a probe current of 0.253 nA. High-angle annular dark field-scanning transmission electron microscopy (HAADF-STEM) and electron energy loss spectroscopy (EELS) elemental mapping measurements were performed at 300 kV on a JEM-ARM300F electron microscope equipped with a spherical aberration corrector. X-ray diffraction (XRD) measurements were conducted using a Bruker D2 PHASER diffractometer with  $\text{Cu K}\alpha$  radiation ( $\lambda = 1.54178\text{ \AA}$ ). X-ray photoelectron spectra (XPS) were recorded on a Thermo Scientific K-alpha spectrometer with an Al  $\text{K}\alpha$  radiation as the excitation source (1486.6 eV). XPS depth profile analysis was conducted by  $\text{Ar}^+$  plasma etching under 1000 eV for 20 s. Brunauer-Emmett-Teller (BET) specific surface areas (measured at  $-196\text{ }^\circ\text{C}$ ), pore width distributions (based on the quenched solid density functional theory), and  $\text{CO}_2$  adsorption capacities (measured at  $25\text{ }^\circ\text{C}$ ) of samples were obtained by using a Quantachrome Autosorb-iQ physical sorption apparatus. Contact angles were recorded on a DSA-X optical contact angle apparatus in ambient air at room temperature. Attenuated total reflectance-surface enhanced infrared absorption spectroscopy (ATR-SEIRAS) measurements were conducted on a Thermo Scientific Nicolet iS20 FT-IR spectrometer equipped with a mercury-cadmium-telluride (MCT) detector.

### 2.5. Electrochemical measurements

**H-type cell:**  $\text{CO}_2$  gas was continuously passed into the cathode chamber of the cell at a flow rate of  $10\text{ mL min}^{-1}$  during electrochemical tests. All potentials mentioned in this work were converted into the RHE scale by the following equation:

$$E(\text{RHE}) = E(\text{Ag/AgCl}) + 0.1989\text{ V} + 0.0592 \times \text{pH} \quad (2)$$

Cyclic voltammetry (CV) measurements were made in the  $\text{CO}_2$ -saturated 0.5 M  $\text{KHCO}_3$  with a potential range of 1 to  $-1\text{ V}$  and a scan rate of  $50\text{ mV s}^{-1}$ . Chronoamperometric measurements were performed in a potential range of  $-0.7$  to  $-1.2\text{ V}$ . Electrochemical surface area

(ECSA) was calculated by the double-layer capacitance ( $C_{dl}$ ) method, which was measured by conducting CV experiments at various scan rates in a potential window of non-faradic area from 0 to  $-0.3\text{ V}$ . Electrochemical impedance spectroscopy (EIS) experiments were carried out at an open-circuit potential from  $1 \times 10^5$  to  $1 \times 10^{-2}\text{ Hz}$  with an amplitude of 5 mV.

**Flow cell:** The flow cell contained a gas chamber, a cathode chamber, and an anode chamber, where the anode and cathode chambers were separated by an anion exchange membrane (FAB-PK-130); the cathode and gas chambers were separated by a gas diffusion electrode. Platinum sheet and Ag/AgCl (3.5 M KCl) electrode were used as counter and reference electrodes, respectively. 1 M KOH was employed as the electrolyte for both the anode and cathode. In the electrochemical testing, a gas flow controller was used to control the continuous flow of  $\text{CO}_2$  gas into the gas chamber at  $20\text{ mL min}^{-1}$ , while two peristaltic pumps were used to circulate the electrolyte at the cathode and anode at  $20\text{ mL min}^{-1}$ . The solution resistance ( $R_s$ ) of the flow cell system was 5–7  $\Omega$  obtained from the EIS tests, and the potentials after ohmic drop compensation were converted to the RHE scale by the following equation:

$$E(iR\text{ corrected RHE}) = E(\text{RHE}) - iR_s \quad (3)$$

### 2.6. Product analysis

Gas-phase products and alcohol liquid-phase products were quantitatively analyzed by gas chromatography (GC, Agilent 7890B), which was equipped with two flame ionization detectors, a thermal conductivity detector, and a headspace injector. Formate and acetate liquid-phase products were detected by high-performance liquid chromatography (HPLC, Agilent 1260 infinity II) equipped with a diode array detector. For quantitative analysis of formate and acetate, 50  $\mu\text{L}$  electrolyte after electrochemical measurements and 100  $\mu\text{L}$  HCl (1 M) were added to 1 mL of deionized water.

### 2.7. Faradaic efficiency calculations

The faradaic efficiency of each reduction product was calculated by the following equation:

$$\text{FE} = \frac{znF}{Q} \times 100\% \quad (4)$$

where  $z$  is the number of electrons required to generate a molecular product;  $n$  is the moles of a product;  $F$  is the Faraday constant ( $96485\text{ C mol}^{-1}$ );  $Q$  is the total charge passing through the working electrode.

### 2.8. Computational methods

Density functional theory (DFT) calculations were conducted using the Vienna Ab initio Simulation Package (VASP) with the generalized gradient approximation (GGA) of Perdew-Burke-Ernzerhof (PBE) to the exchange-correlation functional [37–40]. The projector-augmented-wave (PAW) method was utilized to describe the electron-ion interactions. The electron wave function was expanded in a plane-wave basis set with a kinetics energy cutoff of 450 eV. For the C/Cu/PTFE-0.05-R model, the  $\text{Cu}_2\text{O}$  (111) surface was used to represent the  $\text{Cu}_2\text{O}$  crystal exposed on the surface of its *ex-Cu* $_2\text{O}/in\text{-Cu}$  heterostructure, while the Cu (111) surface located inside the  $\text{Cu}_2\text{O}$  (111) surface was used to represent the  $\text{Cu}^0$  crystal encapsulated by the surface  $\text{Cu}_2\text{O}$  crystal. Given that the heterostructure of C/Cu-0.05-R is opposite to that of C/Cu/PTFE-0.05-R, we used the Cu (111) surface to represent the Cu crystal exposed on the surface of the former, while the  $\text{Cu}_2\text{O}$  (111) surface located inside Cu (111) surface was used to represent its internal  $\text{Cu}_2\text{O}$  crystal. In addition, the Cu (111) surface and  $\text{Cu}_2\text{O}$  (111)



surface were also used to symbolize the models of pure metallic  $\text{Cu}^0$  and pure  $\text{Cu}_2\text{O}$  catalysts, respectively. Vacuum region layers were built more than 20 Å to avoid the interaction between neighboring supercells. The Brillouin zones were sampled with  $3 \times 3 \times 1$  k-point mesh. When the energy change was smaller than  $10^{-6}$  eV, the electronic energy was considered self-consistent. The force convergence criterion for the relaxation was  $0.02 \text{ eV } \text{\AA}^{-1}$ .

The adsorption energy (AE) of an adsorbate was calculated based on the following equation:

$$AE = E_{\text{total}} - E_{\text{surf}} - E_{\text{ad}} \quad (5)$$

where  $E_{\text{total}}$ ,  $E_{\text{surf}}$ , and  $E_{\text{ad}}$  are the total energy of the adsorbate binding to surface, the energy of clean surface, and the energy of free adsorbate in vacuum, respectively.

The Gibbs free energy ( $G$ ) for each elementary step was calculated based on the computational hydrogen electrode model according to the following equation:

$$G = E_{\text{DFT}} + E_{\text{ZPE}} + \int C_V dT - TS \quad (6)$$

where  $E_{\text{DFT}}$  is the energy obtained from DFT calculations;  $E_{\text{ZPE}}$  is the zero-point energy;  $\int C_V dT$  is the heat capacity,  $TS$  is the energy contributed by entropy [41]. Half of Gibbs free energy of a  $\text{H}_2$  molecule is assumed to be the Gibbs free energy contribution of an electron-proton pair [42].

### 3. Results and discussion

#### 3.1. Preparation and characterization of heterostructured $\text{Cu}^0\text{-Cu}_2\text{O}$ catalysts

The preparation procedure of heterostructured  $\text{Cu}^0\text{-Cu}_2\text{O}$  nanoparticles is illustrated in Fig. 1. Briefly, we uniformly covered the surface of porous coal matrix with  $\text{Cu}_x\text{O}$  obtained by a chemical reduction method (reducing agent: ascorbic acid) and then wrapped PTFE on the outer surface of  $\text{Cu}_x\text{O}$ . The synthesized  $\text{Cu}_x\text{O}$  precursor is called C/ $\text{Cu}$ /PTFE- $x$ , where  $x$  represents the amount of ascorbic acid used. Subsequently, the  $\text{Cu}_x\text{O}$  precursor underwent an electrochemical reconstruction process and was transformed into the heterostructured  $\text{Cu}^0\text{-Cu}_2\text{O}$  nanoparticles. The as-obtained sample is denoted C/ $\text{Cu}$ /PTFE- $x$ -R, where R means that the sample has undergone the reconstruction process.

We first measured the  $\text{N}_2$  adsorption and desorption isotherms of porous coal (PC) and  $\text{Cu}_x\text{O}$  precursors. As shown in Fig. S1, PC exhibits the Type I isotherm and has the relatively high  $\text{N}_2$  adsorption capacity, signifying that we successfully prepared a good number of micropores on the surface of the coal matrix by the chemical activation, which is beneficial for anchoring Cu species [43,44]. The  $\text{N}_2$  adsorption capacities of the  $\text{Cu}_x\text{O}$  precursors are substantially lower compared to that of PC, which implies that the  $\text{Cu}_x\text{O}$  species are successfully anchored in the pores of the coal matrix. The specific surface area (SSA) and pore volume of each sample are presented in Table S2. Notably, C/ $\text{Cu}$ /PTFE-0.05 and C/ $\text{Cu}$ -0.05 have similar pore volumes and SSAs, both of which are much smaller than those of PC, indicating that the  $\text{Cu}_x\text{O}$  species encapsulates

the coal matrix tightly and fills the microporous structure of the coal matrix whereas PTFE is distributed around the coal matrix and  $\text{Cu}_x\text{O}$  species.

Next, we characterized the morphology and crystal structure of each sample by TEM. As presented in Figs. 2a and S2a, the  $\text{Cu}_x\text{O}$  coating covers the surface of the coal matrix while PTFE wraps around the periphery of the  $\text{Cu}_x\text{O}$  coating in C/ $\text{Cu}$ /PTFE-0.05, consistent with the above SSA results. The EDS elemental mapping images in Figs. 2d-g and S3a,b exhibit the distributions of C, Cu, O and F elements in C/ $\text{Cu}$ /PTFE-0.05. It is obvious that the coal-matrix surface possesses the high concentrations and uniform distributions of Cu and O, which further manifests that the  $\text{Cu}_x\text{O}$  coating is evenly covered on the coal matrix [45]. In addition, the relatively high concentration of elemental F around the coal matrix proves that PTFE is indeed wrapped around the coal matrix and  $\text{Cu}_x\text{O}$  coating. The HAADF-STEM images show crystals with lattice spacings of  $0.24 \pm 0.01$  and  $0.23 \pm 0.01$  nm in the  $\text{Cu}_x\text{O}$  coating (Fig. 2b,c and S4), indicating that the  $\text{Cu}_x\text{O}$  coating is composed of  $\text{Cu}_2\text{O}$  and/or  $\text{CuO}$  crystals [46,47]. In order to construct the  $\text{Cu}^0\text{-Cu}_2\text{O}$  heterostructure, the  $\text{Cu}_x\text{O}$  precursors are electrolyzed in the ECR system for 30 min (at  $-1.0$  V) by the electrochemical reconstruction method. Fig. S5 displays the CV curves of each  $\text{Cu}_x\text{O}$  precursor in the  $\text{CO}_2$ -saturated  $\text{KHCO}_3$  solution. Clearly, they show reduction peaks at 0.47 and 0.24 V, which indicate that the Cu species in these samples experience the sequential transitions from  $\text{CuO}$  to  $\text{Cu}_2\text{O}$  and then from  $\text{Cu}_2\text{O}$  to  $\text{Cu}^0$  at these two reduction potentials. The relatively positive reduction potential of  $\text{CuO}$  (0.47 V) suggests that  $\text{CuO}$  can rapidly be converted to OD Cu [19]. Fig. 2h and S2b show the morphology of the reconstructed C/ $\text{Cu}$ /PTFE-0.05-R. The original  $\text{Cu}_x\text{O}$  coating is transformed into the nanoparticulate structure (marked with the dark blue area in Fig. 2h and

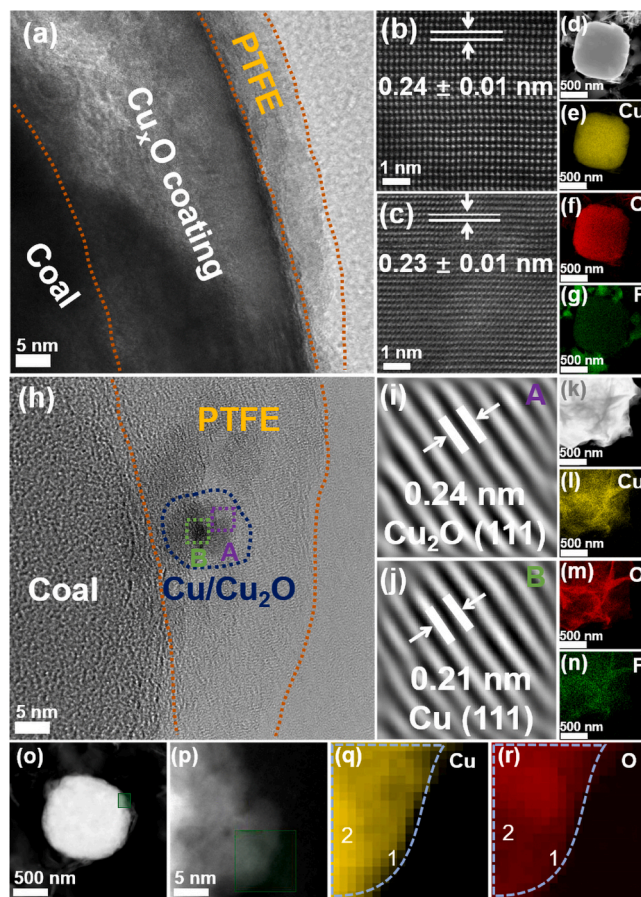


Fig. 2. (a) TEM, (b, c) HAADF-STEM, and (d-g) EDS elemental mapping images of C/ $\text{Cu}$ /PTFE-0.05. (h) TEM, (i, j) lattice fringes, (k-n) EDS elemental mapping images, and (o-r) EELS elemental mapping images of C/ $\text{Cu}$ /PTFE-0.05-R.

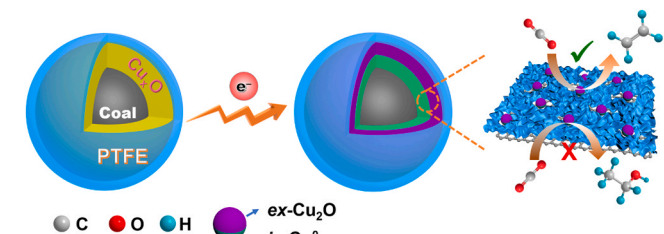


Fig. 1. Schematic diagram of the preparation process of the C/ $\text{Cu}$ /PTFE-series samples, ex: external; in: internal.

S6). Fig. 2i,j exhibit the lattice fringes of the two adjacent regions of A (purple) and B (green) of the nanoparticles in Fig. 2h, respectively. The lattice spacings in the A and B regions are measured to be 0.24 and 0.21 nm (Fig. S7), which originate from the  $\text{Cu}_2\text{O}$  (111) and metallic  $\text{Cu}^0$  (111) surfaces, respectively [46]. Therefore, these results strongly demonstrate that the electrochemical reconstruction process succeeds in converting the  $\text{Cu}_x\text{O}$  precursor to the heterostructured  $\text{Cu}^0\text{-Cu}_2\text{O}$  nanoparticles on the surface of coal matrix. It is worth noting that PTFE is still stably wrapped around the coal matrix and  $\text{Cu}^0\text{-Cu}_2\text{O}$  nanoparticles, indicating that PTFE effectively protects the  $\text{Cu}_2\text{O}$  species on the sample surface from further electroreduction during the reconstruction process. Fig. 2k-n and S3c,d show the EDS elemental mapping images of C/Cu/PTFE-0.05-R. The uniform elemental distributions of Cu, O and F on the coal matrix not only evidence that the  $\text{Cu}^0\text{-Cu}_2\text{O}$  nanoparticles are evenly distributed on the coal matrix but also prove that PTFE adheres to the sample surface firmly. As a result, PTFE can provide a protective role for the  $\text{Cu}^0\text{-Cu}_2\text{O}$  nanoparticles, which contributes to enhancing the electrochemical performance stability of the catalyst. To further investigate the distributions of  $\text{Cu}_2\text{O}$  and  $\text{Cu}^0$  in C/Cu/PTFE-0.05-R, we measured its EELS elemental mapping (Figs. 2o-r and S8) [48]. Notably, the concentration of elemental Cu at the edge (position 1) is lower than in the interior (position 2), indicating that the content of Cu species is smaller at the edge of the sample than inside. On the other hand, the concentration of O at the edge (position 1) is almost the same as that inside (position 2), which suggests that  $\text{Cu}_2\text{O}$  is uniformly distributed on the outer surface of the sample. Thus, based on the elemental distributions of Cu and O, it can be demonstrated that the Cu species at the edge of the sample is  $\text{Cu}_2\text{O}$ , while  $\text{Cu}^0$  is located inside  $\text{Cu}_2\text{O}$  (which are discussed in more detail in Fig. S9).

Fig. S10-S13 present the TEM and elemental mapping images of a series of control samples including C/Cu/PTFE-0.01 and C/Cu/PTFE-0.1 with different ascorbic acid usages, Cu/PTFE-0.05 without the coal matrix, and C/Cu-0.05 without PTFE before and after the electrochemical reconstruction. The lattice fringes of the  $\text{Cu}_2\text{O}$  (111) and  $\text{Cu}^0$  (111) surfaces can clearly be observed in the TEM images of the reconstructed samples, but no lattice fringe of the  $\text{CuO}$  (111) surface can be found, which indicates that all  $\text{Cu}_x\text{O}$  precursors are transformed into

the  $\text{Cu}^0\text{-Cu}_2\text{O}$  nanoparticulate structure after the electrochemical reconstruction.

To further explore the crystal structures of the Cu species in the as-obtained samples, we measured their XRD patterns. Fig. 3a shows the XRD patterns of each  $\text{Cu}_x\text{O}$  precursor. With the increase in ascorbic acid usage, the intensities of  $\text{CuO}$  diffraction peaks gradually decrease, while those of  $\text{Cu}_2\text{O}$  diffraction peaks gradually increase. These phenomena suggest that the crystallinity of  $\text{CuO}$  decreases with increasing the use of ascorbic acid, while the  $\text{Cu}_2\text{O}$  crystals show the opposite trend, implying that the amount of ascorbic acid can regulate the crystal composition of the  $\text{Cu}_x\text{O}$  precursors [49]. The diffraction peak intensities of the Cu species for both C/Cu/PTFE-0.05 and C/Cu-0.05 are higher than that of C/Cu/PTFE-0.05. This indicates that both coal matrix and PTFE possess the spatial confinement effect, which can lower the agglomeration degree of the Cu species. The XRD patterns of the electrochemically reconstructed catalysts are presented in Fig. 3b. Noticeably, the intensities of  $\text{CuO}$  diffraction peaks in all samples become very weak, while those of  $\text{Cu}_2\text{O}$  diffraction peaks are relatively strong. The diffraction peaks of metallic  $\text{Cu}^0$  (111) and (200) surfaces appear at  $43.2^\circ$  and  $50.3^\circ$  for each sample, respectively [50]. These results vividly demonstrate that we have indeed transformed the  $\text{Cu}_x\text{O}$  precursors into the  $\text{Cu}^0\text{-Cu}_2\text{O}$  nanoparticulate structure by the electrochemical reconstruction method, consistent with the TEM observations. It is worth noting that C/Cu-0.05-R possesses the strongest  $\text{Cu}^0$  diffraction peak intensity, implying that it has the highest  $\text{Cu}^0$  crystallinity, which also demonstrates that its Cu species are rapidly converted to  $\text{Cu}^0$  without the PTFE protection in the electrolysis process. Thus, PTFE is essential for stabilizing the chemical state of Cu species. On the other hand, since the spatial confinement effect of the microporous structure of coal matrix contributes to stabilizing the chemical state of the Cu species in the micropores [21], C/Cu-0.05-R can retain small quantities of  $\text{CuO}$  and  $\text{Cu}_2\text{O}$  species in its pores after the reconstruction at the relatively negative electrolysis potential ( $-1\text{ V}$ ). As C/Cu/PTFE-0.05-R has not only the coal matrix with sufficient micropores but also the PTFE protective layer, the chemical state of Cu species in C/Cu/PTFE-0.05-R can remain stable during the prolonged ECR process. Except for C/Cu-0.05-R, the other four samples all exhibit the obvious PTFE

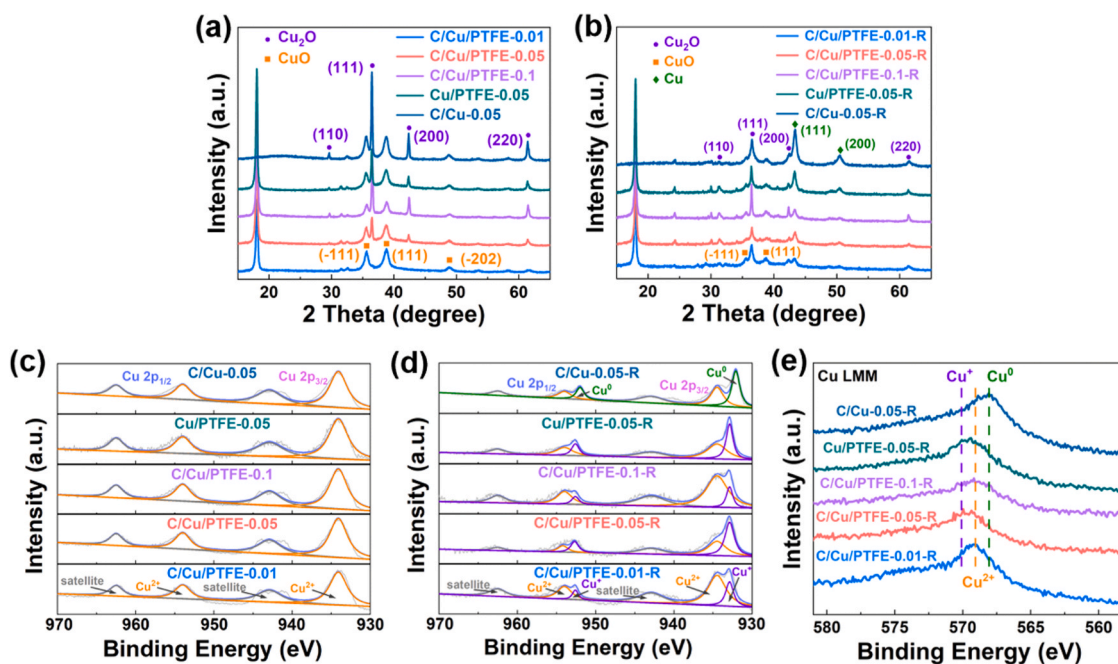


Fig. 3. (a) XRD patterns and (c) high-resolution XPS Cu 2p spectra of C/Cu/PTFE-0.01, C/Cu/PTFE-0.05, C/Cu/PTFE-0.1, Cu/PTFE-0.05, and C/Cu-0.05. (b) XRD patterns, (d) high-resolution XPS Cu 2p spectra and (e) Cu LMM Auger spectra of C/Cu/PTFE-0.01-R, C/Cu/PTFE-0.05-R, C/Cu/PTFE-0.1-R, Cu/PTFE-0.05-R, and C/Cu-0.05-R.

diffraction peaks at  $18^\circ$  before and after the reconstruction (Figs. 3a,b and S14) [27], which also evidences that PTFE can maintain the excellent stability during the electrochemical process.

We then measured the compositions of Cu species on the surface of each sample using XPS. Fig. 3c exhibits the high-resolution XPS Cu 2p spectra of the  $\text{Cu}_x\text{O}$  precursors, with the  $\text{Cu}^{2+}$  species peaks (Cu 2p<sub>3/2</sub>: 934.2 eV; Cu 2p<sub>1/2</sub>: 954.0 eV) and the satellite peaks (Cu 2p<sub>3/2</sub>: 942.9 eV; Cu 2p<sub>1/2</sub>: 962.5 eV) [51]. This observation reveals that the Cu species on the surface of each sample is CuO, while  $\text{Cu}_2\text{O}$  is encapsulated inside CuO, and it also suggests that the  $\text{Cu}_2\text{O}$  crystals start nucleation inside CuO and then gradually agglomerate. After the electrochemical reconstruction, the peak pattern of every sample changes significantly. As shown in Fig. 3d, the four samples wrapped with PTFE each display new, evident  $\text{Cu}^+$  species peaks (Cu 2p<sub>3/2</sub>: 932.9 eV; Cu 2p<sub>1/2</sub>: 952.6 eV) [51], whereas C/Cu-0.05-R without PTFE presents new  $\text{Cu}^0$  species peaks (Cu 2p<sub>3/2</sub>: 932.1 eV; Cu 2p<sub>1/2</sub>: 951.8 eV) [52]. The Cu LMM Auger spectra (Fig. 3e) exhibit that the four samples possessing PTFE show two peaks located at about 570 and 569 eV, corresponding to  $\text{Cu}^+$  and  $\text{Cu}^{2+}$ , respectively, which further indicates that the Cu species on their surfaces are composed of  $\text{Cu}_2\text{O}$  and CuO [53]. On the other hand, C/Cu-0.05-R shows a prominent  $\text{Cu}^0$  peak at around 568 eV and a  $\text{Cu}^{2+}$  peak at about 569 eV, but no  $\text{Cu}^+$  peak [53]. These results illustrate that CuO on the surface of all samples is partially converted to  $\text{Cu}_2\text{O}$  during the electrochemical reconstruction process, in which  $\text{Cu}_2\text{O}$  on the surface of C/Cu-0.05-R is further reduced to metallic  $\text{Cu}^0$  due to the lack of PTFE protection.

It is worth mentioning that both TEM and XRD characterization results of C/Cu/PTFE-0.05-R show that its Cu species is mainly composed of  $\text{Cu}_2\text{O}$  and  $\text{Cu}^0$ , but it does not exhibit the  $\text{Cu}^0$  peak in its high-resolution XPS Cu 2p spectrum (Fig. 3d). In addition, the Cu species on the surface of C/Cu/PTFE-0.05-R is dominated by  $\text{Cu}_2\text{O}$  (Table S3). Therefore, it can be concluded from the above results that the Cu species on the surface of C/Cu/PTFE-0.05-R is mainly the  $\text{Cu}_2\text{O}$  crystal, while its  $\text{Cu}^0$  crystal is encapsulated inside  $\text{Cu}_2\text{O}$ . This is because the Cu species on the surface of C/Cu/PTFE-0.05-R can sufficiently be exposed to low-

conductivity PTFE, which is able to decrease the electron accumulation near the  $\text{Cu}_2\text{O}$  species, thus slowing down the reduction kinetics of  $\text{Cu}_2\text{O}$  and maintaining its chemical state. In contrast, the Cu species inside the sample is reduced to  $\text{Cu}^0$  due to its lack of contact with PTFE. Consequently,  $\text{Cu}_2\text{O}$  and  $\text{Cu}^0$  of C/Cu/PTFE-0.05-R are not mixed on its surface but show the heterostructure with external  $\text{Cu}_2\text{O}$  and internal  $\text{Cu}^0$  (denoted *ex*- $\text{Cu}_2\text{O}$ /*in*- $\text{Cu}^0$ , *ex*: external, *in*: internal). In order to exclude the possibility that  $\text{Cu}_2\text{O}$  and CuO on the surface of C/Cu/PTFE-0.05-R are formed by the oxidation of  $\text{Cu}^0$  in the air (considering that the sample is exposed to air during the sonication and collection treatments), we employed the XPS technique with  $\text{Ar}^+$  plasma etching to investigate the elemental composition and chemical state inside the sample [54]. As exhibited in Table S4 and Fig. 4, the O content of C/Cu/PTFE-0.05-R significantly decreases after the  $\text{Ar}^+$  plasma etching, and almost all elemental O exists in the form of Cu-O group in the sample [55], which indicates that the outermost layer of oxides from the sample has been removed. Notably, the content and chemical state of the Cu species hardly change before and after the etching.  $\text{Cu}_2\text{O}$  remains as the dominant Cu species, and no metallic  $\text{Cu}^0$  appears. This phenomenon demonstrates that the electrochemical reconstruction process allows the  $\text{Cu}_2\text{O}$  species to be evenly distributed in the surface layer of C/Cu/PTFE-0.05-R, while the  $\text{Cu}^0$  species is located deep inside the  $\text{Cu}_2\text{O}$  species. At the same time, the absence of  $\text{Cu}^0$  in the surface layer of the sample also indicates that the surface  $\text{Cu}_2\text{O}$  species is not reduced further to  $\text{Cu}^0$  under the protective effect of PTFE during the electrochemical reconstruction process, thereby eliminating the possibility that the surface  $\text{Cu}_2\text{O}$  and CuO are generated due to the surface re-oxidation. On the other hand, C/Cu/PTFE-0.01-R, C/Cu/PTFE-0.1-R, and C/PTFE-0.05-R own the same heterostructure as C/Cu/PTFE-0.05-R due to the PTFE protective layer, but the latter possesses a relatively higher proportion of  $\text{Cu}^+$  species on the surface (Table S3), indicating that low-crystallinity  $\text{Cu}_2\text{O}$  is more easily exposed to the surface, which is thus conducive to increasing the quantities of active sites.  $\text{Cu}^0$  is the dominant Cu species on the surface of C/Cu-0.05-R (Table S3), and the above XRD analysis results show that the Cu species of C/Cu-0.05-R is

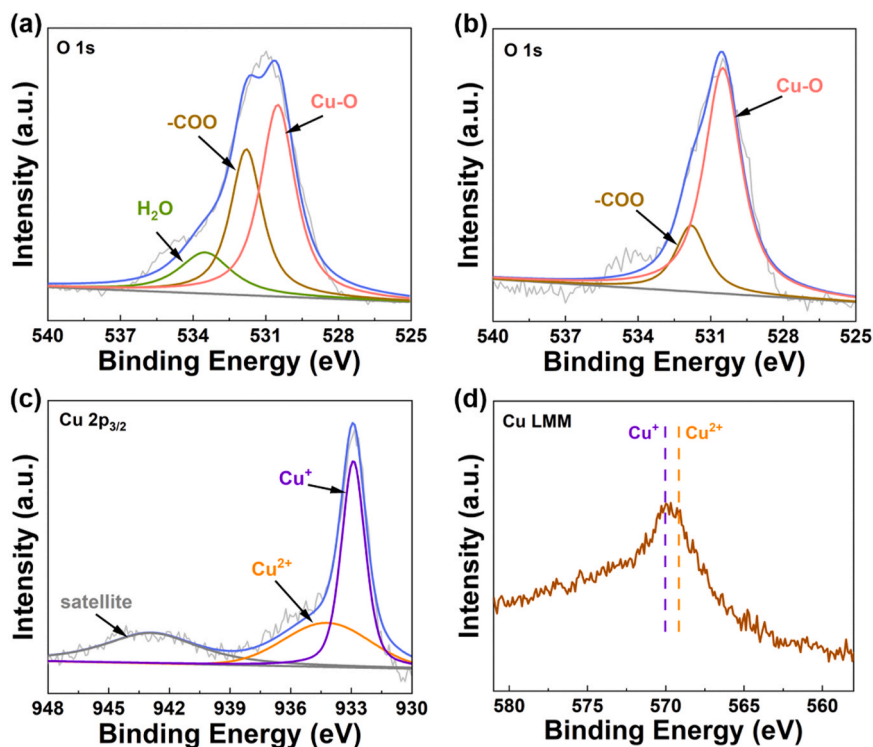


**Fig. 4.** High-resolution XPS O 1s spectra of (a) pristine and (b)  $\text{Ar}^+$  plasma etched C/Cu/PTFE-0.05-R. (c) High-resolution XPS Cu 2p<sub>3/2</sub> spectrum and (d) Cu LMM Auger spectrum of  $\text{Ar}^+$  plasma etched C/Cu/PTFE-0.05-R.



mainly composed of high-crystallinity  $\text{Cu}^0$  and low-crystallinity  $\text{Cu}_2\text{O}$ . These results lead to the conclusion that the Cu species of C/Cu-0.05-R also possesses the heterostructure with external  $\text{Cu}^0$  and internal  $\text{Cu}_2\text{O}$  (denoted *ex-Cu<sup>0</sup>/in-Cu<sub>2</sub>O*).

### 3.2. Electrocatalytic performance

Subsequently, we employed chronoamperometry within a wide potential range of  $-0.7$  to  $-1.2$  V to evaluate faradaic efficiency (FE) and current density ( $j$ ) of reaction products for the as-prepared samples. As displayed in Figs. 5a and S15,  $\text{C}_2\text{H}_4$  and CO are the main ECR products, while  $\text{H}_2$  is the only by-product. The sum of FEs of  $\text{C}_2\text{H}_4$ , CO and  $\text{H}_2$  is almost 100% at each reduction potential, and no other products are detected. In addition, PC only generates  $\text{H}_2$  and CO in the electrochemical measurements (Fig. S16), whereas the pure PTFE material has no current signal due to its poor electrical conductivity. The above results demonstrate that the product  $\text{C}_2\text{H}_4$  does originate from the Cu species in the samples. Moreover, the Cu-based heterostructure that exposes only a single-type  $\text{Cu}_2\text{O}$  crystal or  $\text{Cu}^0$  crystal on its surface enables it to obtain the single deep-reduction product  $\text{C}_2\text{H}_4$ . With the

negative scanning of potentials from  $-0.7$  V, the FE of  $\text{C}_2\text{H}_4$  ( $\text{FE}_{\text{C}_2\text{H}_4}$ ) steadily increases whereas the FE of CO ( $\text{FE}_{\text{CO}}$ ) gradually decreases for each sample. This observation demonstrates that  $\text{CO}_2$  is rapidly reduced to the intermediate  $^*\text{CO}$ , which is then converted to  $\text{C}_2\text{H}_4$  after undergoing a multi-step proton-coupled electron transfer (PCET) process [25]. Remarkably, the maximum  $\text{FE}_{\text{C}_2\text{H}_4}$  of C/Cu/PTFE-0.05-R reaches 44% ( $-1.0$  V), while that of C/Cu-0.05-R is only 21% ( $-0.9$  V), indicating that the *ex-Cu<sub>2</sub>O/in-Cu<sup>0</sup>* heterostructure possesses the superior  $\text{C}_2\text{H}_4$  selectivity to *ex-Cu<sup>0</sup>/in-Cu<sub>2</sub>O*. Fig. 5d shows the  $\text{CO}_2$  adsorption isotherms of the five samples. It is obvious that the  $\text{CO}_2$  adsorption capacity of C/Cu-0.05-R is much higher than those of the other samples, which verifies that PTFE decreases their  $\text{CO}_2$  adsorption capacities. However, the optimum  $\text{FE}_{\text{C}_2\text{H}_4}$  of the four samples coated with PTFE exceeds that of C/Cu-0.05-R (Fig. 5a), which also confirms that the activity of the *ex-Cu<sub>2</sub>O/in-Cu<sup>0</sup>* heterostructure toward the generation of  $\text{C}_2\text{H}_4$  is higher than for the *ex-Cu<sup>0</sup>/in-Cu<sub>2</sub>O* heterostructure. Figs. 5b and S17 show the partial current density of each product for the five samples. C/Cu/PTFE-0.05-R exhibits a relatively large  $j_{\text{C}_2\text{H}_4}$  at all potentials compared with the others, reflecting its excellent tendency for  $\text{C}_2\text{H}_4$ . In addition, the  $j_{\text{C}_2\text{H}_4}$  of C/Cu/PTFE-0.05-R achieves the maximum value

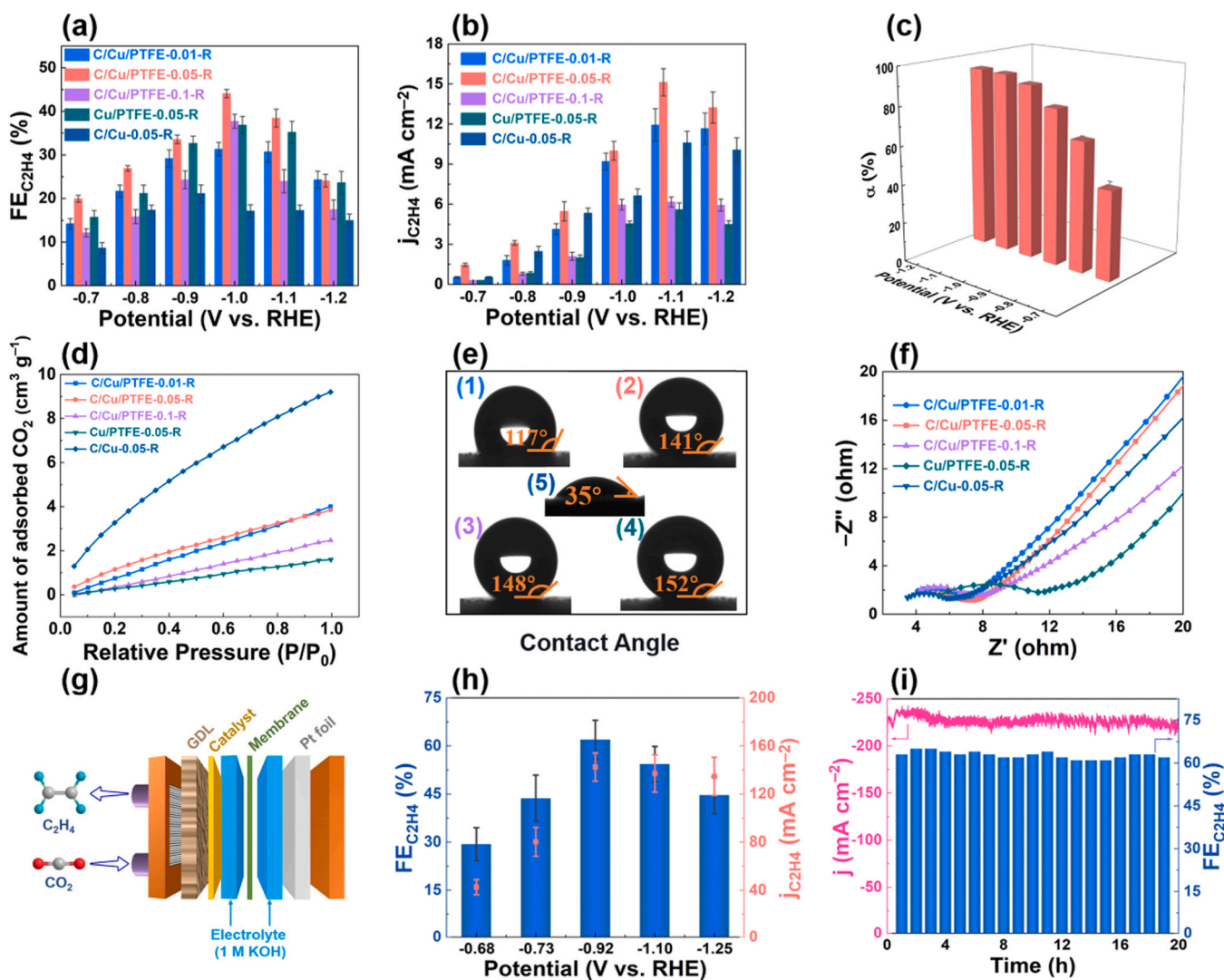


**Fig. 5.** (a)  $\text{FE}_{\text{C}_2\text{H}_4}$  and (b)  $j_{\text{C}_2\text{H}_4}$  of C/Cu/PTFE-0.01-R, C/Cu/PTFE-0.05-R, C/Cu/PTFE-0.1-R, Cu/PTFE-0.05-R and C/Cu-0.05-R at different applied potentials. (c)  $\alpha$  values of C/Cu/PTFE-0.05-R at different applied potentials. (d)  $\text{CO}_2$  adsorption isotherms of C/Cu/PTFE-0.01-R, C/Cu/PTFE-0.05-R, C/Cu/PTFE-0.1-R, Cu/PTFE-0.05-R and C/Cu-0.05-R. (e) Contact angle images of (1) C/Cu/PTFE-0.01-R, (2) C/Cu/PTFE-0.05-R, (3) C/Cu/PTFE-0.1-R, (4) Cu/PTFE-0.05-R and (5) C/Cu-0.05-R. (f) Nyquist plots for C/Cu/PTFE-0.01-R, C/Cu/PTFE-0.05-R, C/Cu/PTFE-0.1-R, Cu/PTFE-0.05-R and C/Cu-0.05-R. (g) Schematic diagram of the flow cell, GDL: gas diffusion layer. (h)  $\text{FE}_{\text{C}_2\text{H}_4}$  and  $j_{\text{C}_2\text{H}_4}$  as a function of potentials for C/Cu/PTFE-0.05-R in the flow cell. (i) Stability assessment of C/Cu/PTFE-0.05-R at  $-0.92$  V (after the iR correction).

(15.1 mA cm<sup>-2</sup>) at -1.1 V, whereas its  $j_{\text{CO}}$  is only 1.1 mA cm<sup>-2</sup> at this potential. Therefore, the smaller  $j_{\text{CO}}$  suggests that most of \*CO generated at the sample surface is further converted to C<sub>2</sub>H<sub>4</sub>. The  $j_{\text{C}_2\text{H}_4}$  of C/Cu/PTFE-0.05-R is much smaller than that of C/Cu/PTFE-0.05-R at -1.1 V, which corroborates that the robust coal matrix can overcome the low-conductivity drawback of Cu/PTFE-0.05-R caused by PTFE and thus significantly enhance its  $j_{\text{C}_2\text{H}_4}$ . Considering that C/Cu/PTFE-0.05-R has the maximum  $j_{\text{C}_2\text{H}_4}$ , we calculated its  $\alpha$  values to quantitatively analyze its tendency to C<sub>2</sub>H<sub>4</sub> in the ECR. As shown in Fig. 5c, the  $\alpha$  values of C/Cu/PTFE-0.05-R are relatively small in the reduction potential range from -0.7 to -0.9 V. Because electric-field strengths at low potentials cannot allow the sample to sufficiently reduce \*CO, a considerable amount of \*CO escapes from electrode surfaces and forms the primitive product CO [23]. When the reduction potential is lower than -0.9 V, the efficient electron/substrate interaction at the Cu<sub>2</sub>O active sites of C/Cu/PTFE-0.05-R makes the catalyst convert most of \*CO to the single deep-reduction product C<sub>2</sub>H<sub>4</sub>, thus achieving the large  $\alpha$  (>90%). Specifically, C/Cu/PTFE-0.05-R achieves an  $\alpha$  value of 93% at -1.1 V, which exceeds the majority of recently reported catalysts (Table S1).

Fig. 5e presents the water contact angles of the five samples. The surface of C/Cu-0.05-R exhibits hydrophilicity (water contact angle < 90°), whereas the surfaces of the four samples possessing PTFE are hydrophobic (water contact angle > 90°). Moreover, the H<sub>2</sub> partial current density ( $j_{\text{H}_2}$ ) of C/Cu-0.05-R is much higher than those of the other samples coated with PTFE (Fig. S17b). The above results demonstrate that PTFE can indeed decrease the proton concentration on the sample surface, thereby effectively diminishing their  $j_{\text{H}_2}$  [27]. Then, we investigated the electrokinetics of each sample using EIS [56]. As exhibited in Fig. 5f, the charge-transfer resistances ( $R_{\text{ct}}$ ) of C/Cu/PTFE-0.01-R, C/Cu/PTFE-0.05-R, C/Cu/PTFE-0.1-R, Cu/PTFE-0.05-R and C/Cu-0.05-R are 3.2, 3.8, 4.5, 6.2 and 2.4  $\Omega$ , respectively, according to the equivalent circuit model (Fig. S18). The relatively large  $R_{\text{ct}}$  of Cu/PTFE-0.05-R indicates low-conductivity PTFE does decrease its charge-transfer rate. The significantly smaller  $R_{\text{ct}}$  values of the samples containing coal reveal that the robust coal matrix has the excellent electrical conductivity, conducive to enhancing current densities of the samples. However, even though C/Cu-0.05-R has a high total current density, its  $j_{\text{H}_2}$  is much larger than its  $j_{\text{C}_2\text{H}_4}$  because the absence of PTFE increases the proton concentration near its active sites. Accordingly, both coal matrix and PTFE are critical for the efficient Cu-based catalyst: the high electrical conductivity of coal allows the catalyst to achieve a high current density, while the hydrophobic PTFE can diminish the energy consumption for side reactions such as HER ( $j_{\text{H}_2}$ ), which in turn yields a high  $j_{\text{C}_2\text{H}_4}$ . After that, we evaluated the ECSAs of the samples by measuring their  $C_{\text{dl}}$  values [57]. As depicted in Fig. S19, C/Cu/PTFE-0.05-R possesses a larger  $C_{\text{dl}}$  than C/Cu/PTFE-0.01-R and C/Cu/PTFE-0.1-R, suggesting the relatively large ECSA value of C/Cu/PTFE-0.05-R, which stems from the high proportion of Cu<sub>2</sub>O crystals on the surface of C/Cu/PTFE-0.05-R providing a large number of active sites. Consequently,  $\text{FE}_{\text{C}_2\text{H}_4}$  and  $j_{\text{C}_2\text{H}_4}$  of C/Cu/PTFE-0.05-R are both better than those of C/Cu/PTFE-0.01-R and C/Cu/PTFE-0.1-R. Additionally, the larger ECSA of C/Cu/PTFE-0.05-R compared to that of Cu/PTFE-0.05-R proves that the porous structure of coal matrix is favorable to elevating the number of active sites. Notably, the ECSA of C/Cu-0.05-R is much greater than that of C/Cu/PTFE-0.05-R, which indicates that PTFE on the surface of the latter does encapsulate its Cu<sup>0</sup>-Cu<sub>2</sub>O nanoparticles, resulting in a relatively small number of active sites. Nevertheless, C/Cu/PTFE-0.05-R possesses the higher  $\text{FE}_{\text{C}_2\text{H}_4}$  and  $j_{\text{C}_2\text{H}_4}$  than C/Cu-0.05-R, demonstrating that the *ex*-Cu<sub>2</sub>O/*in*-Cu<sup>0</sup> heterostructure is more beneficial for the generation of C<sub>2</sub>H<sub>4</sub>.

C/Cu/PTFE-0.05-R shows the excellent C<sub>2</sub>H<sub>4</sub> activity in an H-type cell, but the low solubility and slow diffusion rate of CO<sub>2</sub> in the electrolyte solution restrict the ECR rate of this catalyst [58]. To overcome the CO<sub>2</sub> mass-transport limitation and to evaluate the application potential of C/Cu/PTFE-0.05-R, we further measured its electrochemical performance using a flow cell that allows CO<sub>2</sub> molecules to diffuse

directly to active sites in the form of gas (Fig. 5g) [59]. Fig. 5h and S20 show the FE and  $j$  of C/Cu/PTFE-0.05-R for C<sub>2</sub>H<sub>4</sub>, CO and H<sub>2</sub> at various potentials in the flow cell. Remarkably, C/Cu/PTFE-0.05-R yields the optimal C<sub>2</sub>H<sub>4</sub> activity at the potential of -0.92 V, with its  $\text{FE}_{\text{C}_2\text{H}_4}$  of 62%. More importantly, its  $j_{\text{C}_2\text{H}_4}$  reaches 142.4 mA cm<sup>-2</sup> at this potential, achieving an industrial-grade current density, which reflects its outstanding ECR rate [59]. The excellent  $\text{FE}_{\text{C}_2\text{H}_4}$  and  $j_{\text{C}_2\text{H}_4}$  of C/Cu/PTFE-0.05-R surpasses most of recently reported catalysts (Table S1). We then elevated the electrochemical stability of C/Cu/PTFE-0.05-R at -0.92 V. As exhibited in Fig. 5i, the total current density and  $\text{FE}_{\text{C}_2\text{H}_4}$  of C/Cu/PTFE-0.05-R can remain stable during a prolonged measurement for 20 h, demonstrating its excellent durability and industrialization potential. To confirm the structural stability of C/Cu/PTFE-0.05-R, we made the XRD and XPS measurements after the stability test. As shown in Fig. S21, the diffraction peaks of PTFE, Cu<sub>2</sub>O and Cu<sup>0</sup> of C/Cu/PTFE-0.05-R still maintain the relatively high peak intensities, which not only indicates that PTFE can stably encapsulate the sample during the ECR but also demonstrates that the Cu species in the sample is mainly composed of Cu<sub>2</sub>O and Cu<sup>0</sup> crystals. It is noteworthy that the Cu species in the surface layer of C/Cu/PTFE-0.05-R remains predominantly Cu<sub>2</sub>O whereas no metallic Cu<sup>0</sup> is present (Fig. S22 with Table S3 and S4). These results prove that C/Cu/PTFE-0.05-R can maintain the *ex*-Cu<sub>2</sub>O/*in*-Cu<sup>0</sup> heterostructure at high reduction current density; furthermore, they also confirm that PTFE can indeed stabilize the Cu<sub>2</sub>O species in the surface layer of C/Cu/PTFE-0.05-R, thus enabling the *ex*-Cu<sub>2</sub>O/*in*-Cu<sup>0</sup> heterostructure to efficiently and stably convert CO<sub>2</sub> to C<sub>2</sub>H<sub>4</sub> over an extended period.

### 3.3. Insight into the CO<sub>2</sub>-to-C<sub>2</sub>H<sub>4</sub> mechanism

To explore the reaction mechanism of the conversion of CO<sub>2</sub> to C<sub>2</sub>H<sub>4</sub> on the active sites of C/Cu/PTFE-0.05-R, we employed the ATR-SEIRAS technique to capture reaction intermediates in the ECR process (Fig. S23). As displayed in Fig. 6a, C/Cu/PTFE-0.05-R possesses its prominent \*COOH peak at about 1230 cm<sup>-1</sup>, revealing that the *ex*-Cu<sub>2</sub>O/*in*-Cu<sup>0</sup> heterostructure can efficiently activate CO<sub>2</sub> molecules and convert them to the intermediate \*COOH [31]. It is worth noting that we do not discover \*CO near 2100 cm<sup>-1</sup> but detect the intermediate \*CO\*CHO at around 1140 cm<sup>-1</sup> instead [18]. These observations suggest that the *ex*-Cu<sub>2</sub>O/*in*-Cu<sup>0</sup> heterostructure can rapidly protonate \*CO to \*CHO and induce the C-C coupling reactions between \*CHO and \*CO (Fig. S24). Moreover, C/Cu/PTFE-0.05-R also presents the C<sub>2</sub>H<sub>4</sub> peak at about 940 cm<sup>-1</sup> [18,60], showing that the sample can indeed electrochemically convert CO<sub>2</sub> to C<sub>2</sub>H<sub>4</sub>. It is worth mentioning that no other deep-reduction products as well as their intermediates are detected, which implies that the *ex*-Cu<sub>2</sub>O/*in*-Cu<sup>0</sup> heterostructure possesses the strong tendency toward C<sub>2</sub>H<sub>4</sub> (i.e., the large  $\alpha$  value) in the ECR. Moreover, we only observed the weak \*COOH and \*CO peaks in the ATR-SEIRAS spectra of PC (Fig. S25), which also confirms that the product C<sub>2</sub>H<sub>4</sub> of C/Cu/PTFE-0.05-R absolutely originates from its *ex*-Cu<sub>2</sub>O/*in*-Cu<sup>0</sup> heterostructure. Based on the ATR-SEIRAS results along with the previously reported literature [25], we have proposed the most plausible reaction route to C<sub>2</sub>H<sub>4</sub> in this ECR system (Fig. 6b). A CO<sub>2</sub> molecule is first activated at the Cu<sub>2</sub>O active site and converted to \*COOH, which is then transformed into \*CO after a step of the PCET process. The moderate adsorption strength of the Cu<sub>2</sub>O site to \*CO allows it to protonate \*CO to \*CHO, which forms \*CO\*CHO after binding to \*CO adsorbed at the adjacent Cu<sub>2</sub>O site. Subsequently, \*CO\*CHO undergoes the one-step hydrogenation process to yield \*CHO\*CHO. After the C-C coupling reaction of the two \*CHO, the intermediate changes to \*OHC-CHO in the oxygen-adsorption configuration, which is eventually converted to the product C<sub>2</sub>H<sub>4</sub> after the multi-step PCET process.

Next, we conducted DFT calculations to disclose the underlying reason for the excellent C<sub>2</sub>H<sub>4</sub> activity of the *ex*-Cu<sub>2</sub>O/*in*-Cu<sup>0</sup> heterostructure in C/Cu/PTFE-0.05-R. According to the above characterization



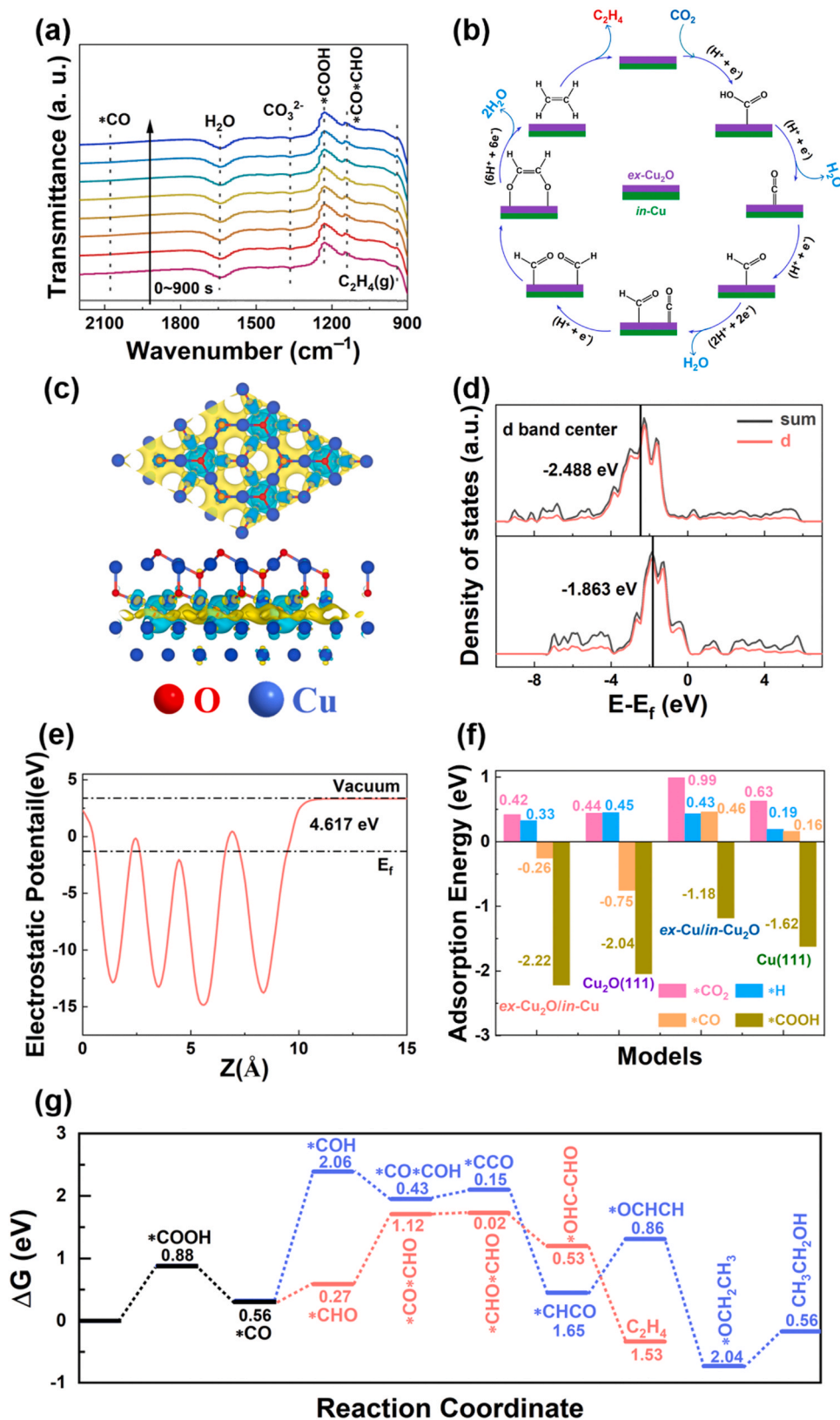


**Fig. 6.** (a) ATR-SEIRAS spectra of C/Cu/PTFE-0.05-R measured at  $-0.8 \text{ V}$ . (b) Proposed reaction mechanism of C/Cu/PTFE-0.05-R for the generation of  $\text{C}_2\text{H}_4$ . (c) Charge-density difference of the  $\text{ex-Cu}_2\text{O}/\text{in-Cu}^0$  model (yellow regions: electron accumulation; cyan regions: electron depletion). (d) Calculated Cu 3d PDOS and TDOS for  $\text{ex-Cu}_2\text{O}/\text{in-Cu}^0$  (upper) and  $\text{Cu}_2\text{O}$  (111) surface (lower). (e) Electrostatic potential work function of  $\text{ex-Cu}_2\text{O}/\text{in-Cu}^0$ . (f) Calculated adsorption energies of reaction intermediates. (g) DFT-calculated Gibbs free energy diagram of  $\text{CO}_2$  reduction to  $\text{C}_2\text{H}_4$  and  $\text{CH}_3\text{CH}_2\text{OH}$  processes on the  $\text{ex-Cu}_2\text{O}/\text{in-Cu}^0$  model.

results, the Cu<sub>2</sub>O (111) surface is used to represent the Cu<sub>2</sub>O species exposed on the C/Cu/PTFE-0.05-R surface, while the Cu (111) surface located inside Cu<sub>2</sub>O (111) is employed to reflect the Cu<sup>0</sup> species encapsulated by Cu<sub>2</sub>O (Fig. S26a) [61,62]. In addition, we constructed the model of the *ex*-Cu<sup>0</sup>/*in*-Cu<sub>2</sub>O heterostructure for C/Cu-0.05-R, where the Cu (111) and Cu<sub>2</sub>O (111) surfaces are located in the upper and lower halves of this model, respectively (Fig. S26b). Moreover, we utilized the Cu<sub>2</sub>O (111) and Cu (111) surfaces to represent the pure Cu<sub>2</sub>O species sample (Fig. S26c) and the pure metallic Cu<sup>0</sup> sample (Fig. S26d), respectively [25,63]. It is evident that O atoms of the Cu<sub>2</sub>O phase and Cu atoms in the Cu phase form the new ionic bonds at the interface of the two phases (Fig. S26a,b), which indicates that Cu<sub>2</sub>O can stably be bonded with metallic Cu<sup>0</sup>.

We carried out charge-density difference analysis to investigate the electron distributions within the *ex*-Cu<sub>2</sub>O/*in*-Cu<sup>0</sup> heterostructure. As shown in Fig. 6c, electrons accumulate at the heterogeneous interface between the Cu<sub>2</sub>O and Cu phases, forming an electron-rich heterogeneous interface. It is known that Cu<sub>2</sub>O is a kind of p-type semiconductor with vacancies whereas metallic Cu<sup>0</sup> has the multiple-electron-transfer property due to its loosely bonded valence electrons [64]. Therefore, when the Cu<sub>2</sub>O phase possessing vacancies and the Cu phase with abundant free electrons constitute the heterostructure, a built-in field is accordingly formed at the heterogeneous interface between the two phases, which induces electrons of the Cu<sub>2</sub>O and Cu phases to move toward the heterogeneous interface, thereby forming the electron-rich heterogeneous interface [65,66]. This situation is akin to the PN junction built by a p-type semiconductor and an n-type semiconductor [67]. Moreover, the Bader charge analysis results show that Cu atoms located on the *ex*-Cu<sub>2</sub>O/*in*-Cu<sup>0</sup> surface are decreased by an average of 0.05 e<sup>-</sup> per atom compared to Cu atoms on the Cu<sub>2</sub>O (111) surface, suggesting that the electron-rich heterogeneous interface of *ex*-Cu<sub>2</sub>O/*in*-Cu<sup>0</sup> lowers the electron density of Cu<sup>+</sup> active sites on its surface. We then calculated the total density of states (TDOS) and the projected density of state (PDOS) of Cu 3d orbitals for *ex*-Cu<sub>2</sub>O/*in*-Cu<sup>0</sup> and Cu<sub>2</sub>O (111) to compare the differences between their electronic states. As shown in Fig. 6d, the electronic states of the Cu 3d orbitals of both samples contribute substantially to their TDOS. Noticeably, the d-band center of surface Cu atoms of *ex*-Cu<sub>2</sub>O/*in*-Cu<sup>0</sup> is negatively shifted compared to the situation of the Cu<sub>2</sub>O (111) surface (from -1.863 to -2.488 eV) and away from the Fermi level, suggesting that the electron-rich heterogeneous interface decreases the local electron density of Cu 3d orbitals of the Cu<sub>2</sub>O phase in *ex*-Cu<sub>2</sub>O/*in*-Cu<sup>0</sup>. According to the above analysis results, it can be concluded that the electron-rich heterogeneous interface formed inside *ex*-Cu<sub>2</sub>O/*in*-Cu<sup>0</sup> effectively modulates the local electron density of 3d orbitals of the Cu<sup>+</sup> active sites in the Cu<sub>2</sub>O phase surface and shifts its d-band center. It is worth noting that adjusting the d-band center of the sample can optimize the binding strength of its active sites to the \*CO intermediate and subsequently enhance its catalytic activity [68]. After that, we calculated the work functions of the four models to study the energy required for electrons transferring from the interiors of these models to their surfaces [66]. As presented in Fig. 6e and S27, *ex*-Cu<sub>2</sub>O/*in*-Cu<sup>0</sup> possesses the smallest work function value, which may be attributed to the plentiful vacancies in its Cu<sub>2</sub>O phase providing ample transport channels for electrons in its heterogeneous interface. Meanwhile, it is also revealed that electrons of the electron-rich heterogeneous interface are able to move freely in the lattice of C/Cu/PTFE-0.05-R and can easily be delivered to the active sites on its Cu<sub>2</sub>O crystal surface, which in turn promotes the ECR.

Then, we calculated the adsorption energies of \*CO<sub>2</sub>, \*H, \*COOH and \*CO on the surfaces of *ex*-Cu<sub>2</sub>O/*in*-Cu<sup>0</sup>, *ex*-Cu<sup>0</sup>/*in*-Cu<sub>2</sub>O, Cu<sub>2</sub>O (111) and Cu (111). As depicted in Fig. 6f, *ex*-Cu<sub>2</sub>O/*in*-Cu<sup>0</sup> and Cu<sub>2</sub>O (111) have the similar adsorption strengths for \*CO<sub>2</sub> and \*COOH, but both of them are significantly stronger than *ex*-Cu<sup>0</sup>/*in*-Cu<sub>2</sub>O and Cu (111), implying that the Cu<sub>2</sub>O species can more efficiently adsorb and transform CO<sub>2</sub> than Cu<sup>0</sup>. In addition, the adsorption energies of *ex*-Cu<sup>0</sup>/*in*-Cu<sub>2</sub>O and Cu (111) for \*CO<sub>2</sub> are far more positive than their adsorption energies for

\*H, which indicates that the Cu<sup>0</sup> species is inclined to adsorb and activate \*H [69]. Therefore, the HER performance of C/Cu-0.05-R with the high-crystallinity Cu<sup>0</sup> crystals exposed on its surface is superior to its ECR counterpart. Furthermore, the \*CO adsorption strength of *ex*-Cu<sub>2</sub>O/*in*-Cu<sup>0</sup> is obviously lower than that of Cu<sub>2</sub>O (111). This behavior demonstrates that modulating the electronic structure of the Cu<sup>+</sup> active sites by the electron-rich heterogeneous interface can break the linear scale relationship and then optimize the adsorption strength of \*CO on the sample surface [70]. If the adsorption strength of active sites to \*CO is too strong, the \*CO poisoning will take place and thus lead to the loss of catalytic capability [71]. As a consequence, the moderate adsorption strength of the active sites for \*CO is conducive to its efficient protonation of \*CO to \*CHO and the generation of C<sub>2</sub>H<sub>4</sub>.

We also calculated the Gibbs free energies of the intermediates on the surfaces of *ex*-Cu<sub>2</sub>O/*in*-Cu<sup>0</sup>, *ex*-Cu<sup>0</sup>/*in*-Cu<sub>2</sub>O, Cu<sub>2</sub>O (111) and Cu (111) according to the above-proposed ECR mechanism for the production of C<sub>2</sub>H<sub>4</sub>. As exhibited in Fig. 6g and S28, the Gibbs free energy change of CO<sub>2</sub>-to-\*COOH transformation ( $\Delta G^{*COOH}$ ) on *ex*-Cu<sub>2</sub>O/*in*-Cu<sup>0</sup> is 0.88 eV, which is similar to that on Cu<sub>2</sub>O (111) (1.06 eV) but significantly smaller than those on *ex*-Cu/*in*-Cu<sub>2</sub>O (1.92 eV) and Cu (111) (1.47 eV). These results manifest that the Cu<sub>2</sub>O species indeed possesses the superior electrocatalytic activity to Cu<sup>0</sup>, so the former is more suitable as the active sites for the ECR. Because Cu<sub>2</sub>O (111) possesses a comparatively large adsorption strength for \*CO, the energy barrier for the protonation of \*CO to \*CHO ( $\Delta G^{*CHO}$ ) on the surface of Cu<sub>2</sub>O (111) is as high as 1.04 eV. In contrast,  $\Delta G^{*CHO}$  on *ex*-Cu<sub>2</sub>O/*in*-Cu<sup>0</sup> is only 0.27 eV due to its moderate adsorption strength for \*CO. These comparisons demonstrate that the electron-rich heterogeneous interface of *ex*-Cu<sub>2</sub>O/*in*-Cu<sup>0</sup> modulating the adsorption strength of Cu<sup>+</sup> active sites for \*CO can significantly promote the protonation reaction of \*CO. In addition, for the \*CO\*CHO → \*CHO\*CHO step, the change of Gibbs free energy for *ex*-Cu<sub>2</sub>O/*in*-Cu<sup>0</sup> (0.02 eV) is much smaller than for Cu<sub>2</sub>O (111) (1.42 eV). This also shows that \*CO is more easily protonated to \*CHO on *ex*-Cu<sub>2</sub>O/*in*-Cu<sup>0</sup>, which can thus accelerate the generation of C<sub>2</sub>H<sub>4</sub>. Moreover, we calculated the CO<sub>2</sub>-to-CH<sub>3</sub>CH<sub>2</sub>OH pathway as well as the Gibbs free energies of the reaction intermediates (Fig. 6g). Notably, the energy barrier of \*CO protonation to \*COH (the key intermediate for CH<sub>3</sub>CH<sub>2</sub>OH) on the surface of *ex*-Cu<sub>2</sub>O/*in*-Cu<sup>0</sup> ( $\Delta G^{*COH}$ ) is as high as 2.06 eV, which is much larger than  $\Delta G^{*CHO}$  (0.27 eV), corroborating that C<sub>2</sub>H<sub>4</sub> is more thermodynamically favorable on the surface of *ex*-Cu<sub>2</sub>O/*in*-Cu<sup>0</sup> than CH<sub>3</sub>CH<sub>2</sub>OH. In addition, the energy barrier for the \*CO protonation to \*COH is also greater than that for its protonation to \*CHO on the *ex*-Cu<sup>0</sup>/*in*-Cu<sub>2</sub>O model (Fig. S29). Accordingly, C/Cu/PTFE-0.05-R and C/Cu-0.05-R only generate the single deep-reduction product C<sub>2</sub>H<sub>4</sub> in the electrochemical measurements. Overall, the results of the theoretical calculations are fully consistent with the experimental data, which provides new insights into the efficient production of a single deep-reduction product C<sub>2</sub>H<sub>4</sub> using the Cu-based heterostructure.

#### 4. Conclusion

To summarize, we have successfully constructed the composite catalyst (C/Cu/PTFE-0.05-R) consisting of porous coal matrix, heterostructured Cu<sup>0</sup>-Cu<sub>2</sub>O nanoparticles and hydrophobic PTFE, in which the Cu<sub>2</sub>O crystal is exposed on the catalyst surface while the Cu<sup>0</sup> crystal is encapsulated inside Cu<sub>2</sub>O. PTFE effectively regulates the electrochemical reconstruction process and induces the exposure of only Cu<sub>2</sub>O on the surface, which thus allows the catalyst to yield the single deep-reduction product C<sub>2</sub>H<sub>4</sub> in the ECR process. More importantly, the electron-rich heterogeneous interface formed inside the Cu<sup>0</sup>-Cu<sub>2</sub>O nanoparticles modulates the electron distribution of 3d orbitals of Cu<sup>+</sup> active sites on the surface. This interaction optimizes the adsorption strength of the Cu<sup>+</sup> active sites with \*CO and enables \*CO to be efficiently and directionally converted to \*CHO on the surface of *ex*-Cu<sub>2</sub>O/*in*-Cu<sup>0</sup>, thereby enhancing the activity of the composite material toward

the generation of C<sub>2</sub>H<sub>4</sub>. Additionally, the outstanding hydrophobicity of PTFE along with the excellent conductivity of coal matrix significantly boosts the  $j_{\text{C}_2\text{H}_4}$  of the catalyst. Consequently, C/Cu/PTFE-0.05-R gives rise to a large  $\alpha$  value (reflecting tendency for C<sub>2</sub>H<sub>4</sub>) of 93%, together with a high FE<sub>C<sub>2</sub>H<sub>4</sub></sub> of 62% and a large  $j_{\text{C}_2\text{H}_4}$  of 142.4 mA cm<sup>-2</sup> in the flow cell. This work not only deepens the understanding of modulating the geometric and electronic structures of active sites to enhance electrocatalytic performance but also has important implications for the design of highly active, selective Cu-based catalysts to yield C<sub>2</sub>H<sub>4</sub> via the ECR route.

#### CRedit authorship contribution statement

**Kong Xiao:** Validation, Formal analysis. **Yang Chuangchuang:** Validation, Formal analysis. **Xu Lang:** Writing – review & editing, Writing – original draft, Supervision, Resources, Project administration, Funding acquisition, Conceptualization. **Liu Weiqi:** Writing – review & editing, Writing – original draft, Visualization, Validation, Software, Methodology, Investigation, Formal analysis, Data curation. **Bai Peiyao:** Software, Investigation, Formal analysis. **Wei Shilin:** Visualization, Validation, Formal analysis.

#### Declaration of Competing Interest

The authors declare that they have no known competing financial interests or personal relationships that could have appeared to influence the work reported in this paper.

#### Data availability

Data will be made available on request.

#### Acknowledgements

This work was supported by the grant from the Fundamental Research Funds for the Central Universities (2023ZDPY04).

#### Appendix A. Supporting information

Supplementary data associated with this article can be found in the online version at doi:10.1016/j.apcatb.2024.123831.

#### References

- [1] Z. Yin, J. Yu, Z. Xie, S.-W. Yu, L. Zhang, T. Akauola, J.G. Chen, W. Huang, L. Qi, S. Zhang, Hybrid catalyst coupling single-atom Ni and nanoscale Cu for efficient CO<sub>2</sub> electroreduction to ethylene, *J. Am. Chem. Soc.* 144 (2022) 20931–20938.
- [2] N. Liu, S. Bartling, A. Springer, C. Kubis, O.S. Bokareva, E. Salaya, J. Sun, Z. Zhang, S. Wohlrab, A.M. Abdel-Mageed, H.-Q. Liang, R. Francke, Heterogenized molecular electrocatalyst based on a hydroxo-bridged binuclear copper(II) phenanthroline compound for selective reduction of CO<sub>2</sub> to ethylene, *Adv. Mater.* (2023) 2309526.
- [3] I. Merino-Garcia, S. Castro, A. Irabien, I. Hernández, V. Rodríguez, R. Camarillo, J. Rincón, J. Albo, Efficient photoelectrochemical conversion of CO<sub>2</sub> to ethylene and methanol using a Cu cathode and TiO<sub>2</sub> nanoparticles synthesized in supercritical medium as photoanode, *J. Environ. Chem. Eng.* 10 (2022) 107441.
- [4] I. Merino-Garcia, J. Albo, A. Irabien, Productivity and selectivity of gas-phase CO<sub>2</sub> electroreduction to methane at copper nanoparticle-based electrodes, *Energy Technol.* 5 (2017) 922–928.
- [5] J. Fu, P. Li, Y. Lin, H. Du, H. Liu, W. Zhu, H. Ren, Fight for carbon neutrality with state-of-the-art negative carbon emission technologies, *Eco-Environ. Health* 1 (2022) 259–279.
- [6] W. Zhang, S. Liu, Y. Yang, H. Qi, S. Xi, Y. Wei, J. Ding, Z.-J. Wang, Q. Li, B. Liu, Z. Chen, Exclusive Co-N<sub>4</sub> sites confined in two-dimensional metal-organic layers enabling highly selective CO<sub>2</sub> electroreduction at industrial-level current, *Angew. Chem. Int. Ed.* 62 (2023) e202219241.
- [7] S. Wei, W. Liu, C. Yang, P. Bai, X. Kong, W. Sun, L. Xu, Electronic and geometric modulations of catalysts for electrochemical CO<sub>2</sub> reduction reaction, *Mater. Chem. Front.* 7 (2023) 4723–4743.
- [8] S. Nitopi, E. Bertheussen, S.B. Scott, X. Liu, A.K. Engstfeld, S. Hørch, B. Seger, I.E. L. Stephens, K. Chan, C. Hahn, J.K. Nørskov, T.F. Jaramillo, I. Chorkendorff, Progress and perspectives of electrochemical CO<sub>2</sub> reduction on copper in aqueous electrolyte, *Chem. Rev.* 119 (2019) 7610–7672.
- [9] W. Nie, G.P. Heim, N.B. Watkins, T. Agapie, J.C. Peters, Organic additive-derived films on Cu electrodes promote electrochemical CO<sub>2</sub> reduction to C<sub>2+</sub> products under strongly acidic conditions, *Angew. Chem. Int. Ed.* 62 (2023) e202216102.
- [10] I. Merino-Garcia, J. Albo, J. Solla-Gullón, V. Montiel, A. Irabien, Cu oxide/ZnO-based surfaces for a selective ethylene production from gas-phase CO<sub>2</sub> electroconversion, *J. CO<sub>2</sub> Util.* 31 (2019) 135–142.
- [11] J. Albo, D. Vallejo, G. Beobide, O. Castillo, P. Castano, A. Irabien, Copper-based metal-organic porous materials for CO<sub>2</sub> electrocatalytic reduction to alcohols, *ChemSusChem* 10 (2017) 1100–1109.
- [12] C. Zhu, Y. Song, X. Dong, G. Li, A. Chen, W. Chen, G. Wu, S. Li, W. Wei, Y. Sun, Ampere-level CO<sub>2</sub> reduction to multicarbon products over a copper gas penetration electrode, *Energy Environ. Sci.* 15 (2022) 5391–5404.
- [13] B. Zhang, J. Zhang, M. Hua, Q. Wan, Z. Su, X. Tan, L. Liu, F. Zhang, G. Chen, D. Tan, X. Cheng, B. Han, L. Zheng, G. Mo, Highly electrocatalytic ethylene production from CO<sub>2</sub> on nanodefective Cu nanosheets, *J. Am. Chem. Soc.* 142 (2020) 13606–13613.
- [14] Z. Ma, C. Tsounis, P.V. Kumar, Z. Han, R.J. Wong, C.Y. Toe, S. Zhou, N.M. Bedford, L. Thomsen, Y.H. Ng, R. Amal, Enhanced electrochemical CO<sub>2</sub> reduction of Cu@CuxO nanoparticles decorated on 3D vertical graphene with intrinsic sp<sup>3</sup>-type defect, *Adv. Funct. Mater.* 30 (2020) 1910118.
- [15] Z. Lyu, S. Zhu, M. Xie, Y. Zhang, Z. Chen, R. Chen, M. Tian, M. Chi, M. Shao, Y. Xia, Controlling the surface oxidation of Cu nanowires improves their catalytic selectivity and stability toward C<sub>2+</sub> products in CO<sub>2</sub> reduction, *Angew. Chem. Int. Ed.* 60 (2021) 1909–1915.
- [16] B. Zhang, J. Zhang, Rational design of Cu-based electrocatalysts for electrochemical reduction of carbon dioxide, *J. Energy Chem.* 26 (2017) 1050–1066.
- [17] P. Grosse, A. Yoon, C. Rettenmaier, A. Herzog, S.W. Chee, B.R. Cuenya, Dynamic transformation of cubic copper catalysts during CO<sub>2</sub> electroreduction and its impact on catalytic selectivity, *Nat. Commun.* 12 (2021) 6736.
- [18] C. Liu, X.-D. Zhang, J.-M. Huang, M.-X. Guan, M. Xu, Z.-Y. Gu, In situ reconstruction of Cu-N coordinated MOFs to generate dispersive Cu/Cu<sub>2</sub>O nanoclusters for selective electroreduction of CO<sub>2</sub> to C<sub>2</sub>H<sub>4</sub>, *ACS Catal.* 12 (2022) 15230–15240.
- [19] P. De Luna, R. Quintero-Bermudez, C.-T. Dinh, M.B. Ross, O.S. Bushuyev, P. Todorović, T. Regier, S.O. Kelley, P. Yang, E.H. Sargent, Catalyst electroreduction controls morphology and oxidation state for selective carbon dioxide reduction, *Nat. Catal.* 1 (2018) 103–110.
- [20] Y. Lum, J.W. Ager, Stability of residual oxides in oxide-derived copper catalysts for electrochemical CO<sub>2</sub> reduction investigated with <sup>18</sup>O labeling, *Angew. Chem. Int. Ed.* 57 (2018) 551–554.
- [21] P.-P. Yang, X.-L. Zhang, F.-Y. Gao, Y.-R. Zheng, Z.-Z. Niu, X. Yu, R. Liu, Z.-Z. Wu, S. Qin, L.-P. Chi, Y. Duan, T. Ma, X.-S. Zheng, J.-F. Zhu, H.-J. Wang, M.-R. Gao, S.-H. Yu, Protecting copper oxidation state via intermediate confinement for selective CO<sub>2</sub> electroreduction to C<sub>2+</sub> fuels, *J. Am. Chem. Soc.* 142 (2020) 6400–6408.
- [22] H. Ning, X. Wang, W. Wang, Q. Mao, Z. Yang, Q. Zhao, Y. Song, M. Wu, Cubic Cu<sub>2</sub>O on nitrogen-doped carbon shells for electrocatalytic CO<sub>2</sub> reduction to C<sub>2</sub>H<sub>4</sub>, *Carbon* 146 (2019) 218–223.
- [23] X. Wei, Z. Yin, K. Lyu, Z. Li, J. Gong, G. Wang, L. Xiao, J. Lu, L. Zhuang, Highly selective reduction of CO<sub>2</sub> to C<sub>2+</sub> hydrocarbons at copper/polyaniline interfaces, *ACS Catal.* 10 (2020) 4103–4111.
- [24] R.M. Arán-Ais, F. Scholten, S. Kunze, R. Rizo, B.R. Cuenya, The role of in situ generated morphological motifs and Cu(I) species in C<sub>2+</sub> product selectivity during CO<sub>2</sub> pulsed electroreduction, *Nat. Energy* 5 (2020) 317–325.
- [25] H. Luo, B. Li, J.-G. Ma, P. Cheng, Surface modification of nano-Cu<sub>2</sub>O for controlling CO<sub>2</sub> electrochemical reduction to ethylene and syngas, *Angew. Chem. Int. Ed.* 61 (2022) e202116736.
- [26] I. Merino-Garcia, J. Albo, A. Irabien, Tailoring gas-phase CO<sub>2</sub> electroreduction selectivity to hydrocarbons at Cu nanoparticles, *Nanotechnology* 29 (2018) 014001.
- [27] P. An, L. Wei, H. Li, B. Yang, K. Liu, J. Fu, H. Li, H. Liu, J. Hu, Y.-R. Lu, H. Pan, T.-S. Chan, N. Zhang, M. Liu, Enhancing CO<sub>2</sub> reduction by suppressing hydrogen evolution with polytetrafluoroethylene protected copper nanoneedles, *J. Mater. Chem. A* 8 (2020) 15936–15941.
- [28] L. Li, J. Chen, V.S.S. Mosali, Y. Liang, A.M. Bond, Q. Gu, J. Zhang, Hydrophobicity graded gas diffusion layer for stable electrochemical reduction of CO<sub>2</sub>, *Angew. Chem. Int. Ed.* 61 (2022) e202208534.
- [29] S. Hong, H.G. Abbas, K. Jang, K.K. Patra, B. Kim, B.-U. Choi, H. Song, K.-S. Lee, P.-P. Choi, S. Ringe, J. Oh, Tuning the C<sub>1</sub>/C<sub>2</sub> selectivity of electrochemical CO<sub>2</sub> reduction on Cu-CeO<sub>2</sub> nanorods by oxidation state control, *Adv. Mater.* 35 (2022) 2208996.
- [30] W. Liu, J. Qi, P. Bai, W. Zhang, L. Xu, Utilizing spatial confinement effect of N atoms in micropores of coal-based metal-free material for efficiently electrochemical reduction of carbon dioxide, *Appl. Catal. B Environ.* 272 (2020) 118974.
- [31] W. Liu, S. Wei, P. Bai, C. Yang, L. Xu, Robust coal matrix intensifies electron/substrate interaction of nickel-nitrogen (Ni-N) active sites for efficient CO<sub>2</sub> electroreduction at industrial current density, *Appl. Catal. B Environ.* 299 (2021) 120661.
- [32] J. Albo, M. Perfecto-Irigaray, G. Beobide, A. Irabien, Cu/Bi metal-organic framework-based systems for an enhanced electrochemical transformation of CO<sub>2</sub> to alcohols, *J. CO<sub>2</sub> Util.* 33 (2019) 157–165.
- [33] J. Albo, G. Beobide, P. Castano, A. Irabien, Methanol electrosynthesis from CO<sub>2</sub> at Cu<sub>2</sub>O/ZnO prompted by pyridine-based aqueous solutions, *J. CO<sub>2</sub> Util.* 18 (2017) 164–172.



- [34] J. Albo, A. Irabien, Cu<sub>2</sub>O-loaded gas diffusion electrodes for the continuous electrochemical reduction of CO<sub>2</sub> to methanol, *J. Catal.* 343 (2016) 232–239.
- [35] J. Albo, A. Sáez, J. Solla-Gullón, V. Montiel, A. Irabien, Production of methanol from CO<sub>2</sub> electroreduction at Cu<sub>2</sub>O and Cu<sub>2</sub>O/ZnO-based electrodes in aqueous solution, *Appl. Catal. B Environ.* 176–177 (2015) 709–717.
- [36] Q. Zhu, X. Sun, D. Yang, J. Ma, X. Kang, L. Zheng, J. Zhang, Z. Wu, B. Han, Carbon dioxide electroreduction to C<sub>2</sub> products over copper-cuprous oxide derived from electrosynthesized copper complex, *Nat. Commun.* 10 (2019) 3851.
- [37] G. Kresse, J. Hafner, Ab initio molecular dynamics for liquid metals, *Phys. Rev. B* 47 (1993) 558–561.
- [38] G. Kresse, J. Hafner, Ab initio molecular-dynamics simulation of the liquid-metal-amorphous-semiconductor transition in germanium, *Phys. Rev. B* 49 (1994) 14251–14269.
- [39] G. Kresse, J. Furthmüller, Efficiency of ab-initio total energy calculations for metals and semiconductors using a plane-wave basis set, *Comput. Mater. Sci.* 6 (1996) 15–50.
- [40] G. Kresse, J. Furthmüller, Efficient iterative schemes for ab initio total-energy calculations using a plane-wave basis set, *Phys. Rev. B* 54 (1996) 11169–11186.
- [41] V. Wang, N. Xu, J.-C. Liu, G. Tang, W.-T. Geng, VASPKIT: A user-friendly interface facilitating high-throughput computing and analysis using VASP code, *Comput. Phys. Commun.* 267 (2021) 108033.
- [42] J.K. Nørskov, J. Rossmeisl, A. Logadottir, L. Lindqvist, Origin of the overpotential for oxygen reduction at a fuel-cell cathode, *J. Phys. Chem. B* 108 (2004) 17886–17892.
- [43] J. Qi, B. Jin, W. Liu, W. Zhang, L. Xu, Converting coals into carbon-based pH-universal oxygen reduction catalysts for fuel cells, *Fuel* 285 (2021) 119163.
- [44] J. Qi, W. Liu, T. Huang, P. Bai, S. Wei, C. Yang, X. Kong, L. Xu, Structural evolution and performance enhancement of coal-based metal-free N,P-doped porous carbon electrocatalysts for pH-universal oxygen reduction, *Chem. Eng. Sci.* 280 (2023) 119077.
- [45] H. Yang, Y.-w. Hu, J.-j. Chen, M.-S. Balogun, P.-p. Fang, S. Zhang, J. Chen, Y. Tong, Intermediates adsorption engineering of CO<sub>2</sub> electroreduction reaction in highly selective heterostructure Cu-based electrocatalysts for CO production, *Adv. Energy Mater.* 9 (2019) 1901396.
- [46] J. Sang, P. Wei, T. Liu, H. Lv, X. Ni, D. Gao, J. Zhang, H. Li, Y. Zang, F. Yang, Z. Liu, G. Wang, X. Bao, A reconstructed Cu<sub>2</sub>P<sub>2</sub>O<sub>7</sub> catalyst for selective CO<sub>2</sub> electroreduction to multicarbon products, *Angew. Chem. Int. Ed.* 61 (2022) e202114238.
- [47] Z. Zhang, Y. Yang, W. Li, W. Zhang, M. Liu, Z. Weng, S. Huo, J. Zhang, Boosting carbon monoxide production during CO<sub>2</sub> reduction reaction via Cu-Sb<sub>2</sub>O<sub>3</sub> interface cooperation, *J. Colloid Interface Sci.* 601 (2021) 661–668.
- [48] Z.-Q. Liang, T.-T. Zhuang, A. Seifitokaldani, J. Li, C.-W. Huang, C.-S. Tan, Y. Li, P. D. Luna, C.T. Dinh, Y. Hu, Q. Xiao, P.-L. Hsieh, Y. Wang, F. Li, R. Quintero-Bermudez, Y. Zhou, P. Chen, Y. Pang, S.-C. Lo, L.-J. Chen, H. Tan, Z. Xu, S. Zhao, D. Sinton, E.H. Sargent, Copper-on-nitride enhances the stable electrosynthesis of multi-carbon products from CO<sub>2</sub>, *Nat. Commun.* 9 (2018) 3828.
- [49] L. Xu, L.-P. Jiang, J.-J. Zhu, Sonochemical synthesis and photocatalysis of porous Cu<sub>2</sub>O nanospheres with controllable structures, *Nanotechnology* 20 (2009) 045605.
- [50] D.-L. Meng, M.-D. Zhang, D.-H. Si, M.-J. Mao, Y. Hou, Y.-B. Huang, R. Cao, Highly selective tandem electroreduction of CO<sub>2</sub> to ethylene over atomically isolated nickel-nitrogen site/copper nanoparticle catalysts, *Angew. Chem. Int. Ed.* 60 (2021) 25485–25492.
- [51] R. Yang, J. Duan, P. Dong, Q. Wen, M. Wu, Y. Liu, Y. Li, H. Li, T. Zhai, In situ halogen-ion leaching regulates multiple sites on tandem catalysts for efficient CO<sub>2</sub> electroreduction to C<sub>2+</sub> products, *Angew. Chem. Int. Ed.* 61 (2022) e202116706.
- [52] X. Zhou, J. Shan, L. Chen, B.Y. Xia, T. Ling, J. Duan, Y. Jiao, Y. Zheng, S.-Z. Qiao, Stabilizing Cu<sup>2+</sup> ions by solid solutions to promote CO<sub>2</sub> electroreduction to methane, *J. Am. Chem. Soc.* 144 (2022) 2079–2084.
- [53] S. Zhen, G. Zhang, D. Cheng, H. Gao, L. Li, X. Lin, Z. Ding, Z.-J. Zhao, J. Gong, Nature of the active sites of copper zinc catalysts for carbon dioxide electroreduction, *Angew. Chem. Int. Ed.* 61 (2022) e202201913.
- [54] F. Wang, Z. Miao, J. Mu, Y. Zhao, M. Liang, J. Meng, X. Wu, P. Zhou, J. Zhao, S. Zhuo, J. Zhou, A Ni nanoparticles encapsulated in N-doped carbon catalyst for efficient electroreduction CO<sub>2</sub>: Identification of active sites for adsorption and activation of CO<sub>2</sub> molecules, *Chem. Eng. J.* 428 (2022) 131323.
- [55] W. Zhang, C. Huang, J. Zhu, Q. Zhou, R. Yu, Y. Wang, P. An, J. Zhang, M. Qiu, L. Zhou, L. Mai, Z. Yi, Y. Yu, Dynamic restructuring of coordinatively unsaturated copper paddle wheel clusters to boost electrochemical CO<sub>2</sub> reduction to hydrocarbons, *Angew. Chem. Int. Ed.* 61 (2022) e202112116.
- [56] W. Zhang, C. Yang, W. Liu, H. Wang, S. Wei, J. Qi, P. Bai, B. Jin, L. Xu, Long-range order, short-range disorder: engineering one-dimensional flow channel arrays with hierarchically porous reaction interfaces for electrocatalytic reduction of oxygen, *Appl. Catal. B Environ.* 293 (2021) 120199.
- [57] H. Du, L.-X. Liu, P. Li, Q. Min, S. Guo, W. Zhu, Enriching reaction intermediates in multishell structured copper catalysts for boosted propanol electrosynthesis from carbon monoxide, *ACS Nano* 17 (2023) 8663–8670.
- [58] J. Chen, T. Wang, X. Wang, B. Yang, X. Sang, S. Zheng, S. Yao, Z. Li, Q. Zhang, L. Lei, J. Xu, L. Dai, Y. Hou, Promoting electrochemical CO<sub>2</sub> reduction via boosting activation of adsorbed intermediates on iron single-atom catalyst, *Adv. Funct. Mater.* 32 (2022) 2110174.
- [59] C.M. Gabardo, A. Seifitokaldani, J.P. Edwards, C.-T. Dinh, T. Burdyny, M.G. Kibria, C.P. O'Brien, E.H. Sargent, D. Sinton, Combined high alkalinity and pressurization enable efficient CO<sub>2</sub> electroreduction to CO, *Energy Environ. Sci.* 11 (2018) 2531–2539.
- [60] W. Xie, K. Li, X.-H. Liu, X. Zhang, H. Huang, P-mediated Cu-N<sub>4</sub> sites in carbon nitride realizing CO<sub>2</sub> photoreduction to C<sub>2</sub>H<sub>4</sub> with selectivity modulation, *Adv. Mater.* 35 (2023) 2208132.
- [61] G. Ma, O.A. Syzgantseva, Y. Huang, D. Stoian, J. Zhang, S. Yang, W. Luo, M. Jiang, S. Li, C. Chen, M.A. Syzgantseva, S. Yan, N. Chen, L. Peng, J. Li, B. Han, A hydrophobic Cu/Cu<sub>2</sub>O sheet catalyst for selective electroreduction of CO to ethanol, *Nat. Commun.* 14 (2023) 501.
- [62] W. Liu, P. Zhai, A. Li, B. Wei, K. Si, Y. Wei, X. Wang, G. Zhu, Q. Chen, X. Gu, R. Zhang, W. Zhou, Y. Gong, Electrochemical CO<sub>2</sub> reduction to ethylene by ultrathin CuO nanoplate arrays, *Nat. Commun.* 13 (2022) 1877.
- [63] H.H. Heenen, H. Shin, G. Kastlunger, S. Overa, J.A. Gauthier, F. Jiao, K. Chan, The mechanism for acetate formation in electrochemical CO<sub>2</sub> reduction on Cu: selectivity with potential, pH, and nanostructuring, *Energy Environ. Sci.* 15 (2022) 3978–3990.
- [64] Y.A. Wu, I. McNulty, C. Liu, K.C. Lau, Q. Liu, A.P. Paulikas, C.-J. Sun, Z. Cai, J. R. Guest, Y. Ren, V. Stamenkovic, L.A. Curtiss, Y. Liu, T. Rajh, Facet-dependent active sites of a single Cu<sub>2</sub>O particle photocatalyst for CO<sub>2</sub> reduction to methanol, *Nat. Energy* 4 (2019) 957–968.
- [65] J. Zhu, F. Xia, Y. Guo, R. Lu, L. Gong, D. Chen, P. Wang, L. Chen, J. Yu, J. Wu, S. Mu, Electron accumulation effect over osmium/erlichmanite heterointerfaces for intensified pH-universal hydrogen evolution, *ACS Catal.* 12 (2022) 13312–13320.
- [66] W. Liu, M. Shi, Y. Li, Z. Wu, L. Yang, S. Zhang, X. Xiao, C. Liu, W. Dai, C. Chen, X. Tu, J. Zou, X. Luo, Congregated-electrons-strengthened anchoring and mineralization of gaseous formaldehyde on a novel self-supporting Cu<sub>2-x</sub>Se/Cu<sub>2</sub>O heterojunction photocatalyst under visible lights: A viable mesh for designing air purifier, *Appl. Catal. B Environ.* 312 (2022) 121427.
- [67] H. Wang, R. Niu, J. Liu, S. Guo, Y. Yang, Z. Liu, J. Li, Electrostatic self-assembly of 2D/2D CoWO<sub>4</sub>/g-C<sub>3</sub>N<sub>4</sub> p-n heterojunction for improved photocatalytic hydrogen evolution: built-in electric field modulated charge separation and mechanism unveiling, *Nano Res.* 15 (2022) 6987–6998.
- [68] D. Wei, Y. Wang, C.-L. Dong, Z. Zhang, X. Wang, Y.-C. Huang, Y. Shi, X. Zhao, J. Wang, R. Long, Y. Xiong, F. Dong, M. Li, S. Shen, Decrypting the controlled product selectivity over Ag-Cu bimetallic surface alloys for electrochemical CO<sub>2</sub> reduction, *Angew. Chem. Int. Ed.* 62 (2023) e202217369.
- [69] W. Liu, P. Bai, S. Wei, C. Yang, L. Xu, Gadolinium changes the local electron densities of nickel 3d orbitals for efficient electrocatalytic CO<sub>2</sub> reduction, *Angew. Chem. Int. Ed.* 61 (2022) e202201166.
- [70] Y.J. Sa, C.W. Lee, S.Y. Lee, J. Na, U. Lee, Y.J. Hwang, Catalyst-electrolyte interface chemistry for electrochemical CO<sub>2</sub> reduction, *Chem. Soc. Rev.* 49 (2020) 6632–6665.
- [71] Z. Li, D. He, X. Yan, S. Dai, S. Younan, Z. Ke, X. Pan, X. Xiao, H. Wu, J. Gu, Size-dependent nickel-based electrocatalysts for selective CO<sub>2</sub> reduction, *Angew. Chem. Int. Ed.* 59 (2020) 18572–18577.